

Niki A. Loppi

## **Wall-Modeling for Large Eddy Simulation of Rotating Flows**

**School of Engineering**

Thesis submitted for examination for the degree of Master of  
Science in Technology.

Espoo March 9, 2015

**Thesis supervisor:**

Professor Timo Siikonen

**Thesis advisor:**

Associate professor Julien Bodart, ISAE

Author: Niki A. Loppi

Title: Wall-Modeling for Large Eddy Simulation of Rotating Flows

Date: March 9, 2015

Language: English

Number of pages: 9+68

Department of Applied Mechanics

Minor: Technical Mechanics (Fluid Mechanics)

Code: K3006

Supervisor: Professor Timo Siikonen

Advisor: Associate professor Julien Bodart, ISAE

Flows affected by system rotation are common phenomena in engineering applications as well as in nature. The coordinate transformation into a rotating frame introduces two fictitious accelerations: the Coriolis acceleration and the centrifugal acceleration, which need to be included in the simulation.

In this thesis, a spanwise rotating turbulent channel flow is studied through Large Eddy Simulations (LES). LES is a numerical modeling approach which is based on the decomposition of the turbulence spectrum into dynamically important large scales and homogeneous small scales. In LES, the large scales are resolved directly, while the effects of small-scales are modeled. In turbulent shear flows, the dynamically important scales are highly proportional to the Reynolds number within the inner boundary layer, which causes LES to be almost as expensive as Direct Numerical Simulation. By modeling the inner layer approximately, it is possible to bypass the very strict requirements of wall-resolved LES.

In this thesis, firstly, the DNS case by Kristoffersen & Anderson [1] is reproduced to validate the implemented Coriolis source terms. After, a database for the wall-model analysis is established by performing wall-resolved high Reynolds number simulations with three different rotation rates. The wall-modeling approach by Kawai & Larsson [2] is then tested through an *a priori* analysis in which a stand-alone wall model is applied to wall-resolved results. Based on these results, a rotation correction, which adapts to the stability effects resulting from the system rotation, is proposed. Finally, this new rotation corrected wall-model is validated by performing a Wall-Modeled Large Eddy Simulation (WMLES). The WMLES results were found to be in good agreement with the wall-resolved data.

Keywords: CFD, LES, wall-modeling, turbulence, system rotation, Coriolis stability, channel flow

Tekijä: Niki A. Loppi		
Työn nimi: Seinämämallinnus pyöriville virtauksille suurten pyörteiden menetelmässä		
Päivämäärä: March 9, 2015	Kieli: Englanti	Sivumäärä: 9+68
Sovelletun Mekaniikan Laitos		
Sivuaine: Teknillinen Mekaniikka (Virtausmekaniikka)		Koodi: K3006
Valvoja: Professori Timo Siikonen		
Ohjaaja: Apulaisprofessori Julien Bodart, ISAE		
<p>Pyörivät virtaukset ovat tavallisia niin teknisissä käytännön sovellutuksissa kuin luonnossakin. Koordinaatiston muunnos pyörivään koordinaatistoon synnyttää kaksi näennäskiihtyvyyttä; Coriolis-kiihtyvyyden ja keskipakoiskiihtyvyyden, jotka tulee ottaa huomioon pyörivien virtausten simuloinnissa.</p> <p>Tässä diplomityössä tutkimme poikkisuuntaisesti pyörivää turbulenttia kanavavirtausta suurten pyörteiden menetelmällä (LES). LES on numeerinen mallinnusmenetelmä, joka perustuu turbulenssispektrin jakamiseen dynaamisesti tärkeisiin suuriin skaaloihin ja homogeenisiin pieniin skaaloihin. LES menetelmässä suuret skaalat ratkaistaan suoraan, kun taas pienet skaalat mallinnetaan. Seinämävirtausten yhteydessä suuret skaalat ovat voimakkaasti verranollisia Reynoldsin lukuun sisemmässä rajakerroksessa, mikä tekee LES:in melkein yhtä raskaaksi kuin suoran simuloinnin (DNS). Mallintamalla tämä sisempi rajakerros approksimatiivisesti voimme välttyä seinämaratkaistun LES:in suurilta vaatimuksilta.</p> <p>Tämä diplomityö aloitetaan toistamalla Kristoffersen &amp; Anderssonin [1] DNS simulointi implementoidun Coriolis-lähdetermin validoimiseksi. Tämän jälkeen suoritetaan suuren Reynoldsin luvun seinämaratkaistuja simulointeja kolmella eri pyörimisnopeudella kerätäksemme tietoa seinämämallianalyysia varten. Seinämämallianalyysissa Kawai &amp; Larssonin [2] ehdottamaa mallinnusmenetelmää testataan itsenäisellä seinämämalliohjelmalla, joka käyttää hyväkseen edellä laskettuja tuloksia. Analyysilla saatujen tulosten perusteella ehdotetaan pyörimiskorjaus, joka ottaa huomioon pyörimisestä aiheutuvat stabiliteetti muutokset. Lopuksi tämä pyörimiskorjattu seinämämalli validoidaan suorittamalla simulointi, jossa seinämämalli toimii osana ratkaisua. Seinämämallinnetun simuloinnin tulosten huomattiin vastaavan hyvin seinämaratkaistuja tuloksia.</p>		
Avainsanat: CFD, LES, seinämämallinnus, turbulenssi, pyörivä systeemi, Coriolis-stabiliteetti, kanavavirtaus		

## Preface

I would like to express my deepest gratitude to As.Prof. Julien Bodart for giving me the amazing opportunity to work on this topic and advising me throughout the project. I would also like to thank the entire DAEP staff at ISAE-SUPAERO. It was a privilege to work in such a great environment with true sense of community. The time I stayed in Toulouse was probably the most remarkable single period of my life thus far. I feel that during the course of the project, I gradually progressed from a student into a beginning researcher. A great thank you also goes to Prof. Timo Siikonen. Without his teaching and general guidance, none of this would have been possible.

I also want to extend my appreciation to my friends here in Finland and back in France. Their support and the necessary leisure activities were an enormous source of energy, without which my journey to Master of Science would have been much more turbulent. A special mention goes to Hilal Asan-Liski for proofreading the thesis. Finally, my appreciation towards my parents and their contribution achievements are beyond words. They are to thank for providing the best possible environment and allowing me to seize every opportunity that have brought me here.

Helsinki, 9.3.2015

Niki A. Loppi

# Contents

<b>Abstract</b>	<b>ii</b>
<b>Abstract (in Finnish)</b>	<b>iii</b>
<b>Preface</b>	<b>iv</b>
<b>Contents</b>	<b>v</b>
<b>Symbols and abbreviations</b>	<b>vii</b>
<b>1 Introduction</b>	<b>1</b>
1.1 Simulating Turbulent Flows: Level of Approximation . . . . .	1
1.2 Previous Research . . . . .	3
1.3 Present Research Objectives . . . . .	5
<b>2 Large Eddy Simulation Principles</b>	<b>6</b>
2.1 Scale Decomposition . . . . .	6
2.2 Navier-Stokes Equations . . . . .	8
2.3 Filtered Governing Equations . . . . .	9
2.4 Subgrid-Scale Modeling . . . . .	11
2.4.1 Vreman Model . . . . .	11
2.4.2 SGS Heat Flux . . . . .	12
<b>3 Near-Wall Treatment Approaches for LES</b>	<b>13</b>
3.1 Motivation for Wall-Modeling . . . . .	13
3.2 Wall-Stress Models . . . . .	14
3.2.1 Deardorff Model . . . . .	15
3.2.2 Schumann and Grötzbach Models . . . . .	15
3.2.3 Shifted and Ejection Models . . . . .	16
3.2.4 Auxiliary Grid Approach: TBLE Model . . . . .	17
3.2.5 Dynamic Auxiliary Grid Approaches . . . . .	19
3.3 RANS/LES Hybrids . . . . .	20
<b>4 System Rotation</b>	<b>22</b>
4.1 Coriolis and Centrifugal Accelerations . . . . .	22
4.2 Spanwise Rotating channel: Average Quantities . . . . .	23
4.3 Coriolis Stability . . . . .	25
4.4 Reynolds Stresses . . . . .	27
<b>5 Low Re Simulation: Rotating Frame Validation</b>	<b>29</b>
5.1 Charles <sup>x</sup> solver . . . . .	29
5.2 Setup . . . . .	29
5.3 Post-Processing . . . . .	30
5.4 Results . . . . .	30

<b>6</b>	<b>High Re Simulation: Reference Data for Wall-Model investigation</b>	<b>33</b>
6.1	Setup . . . . .	33
6.2	Results . . . . .	33
6.2.1	Mean Statistics . . . . .	33
6.2.2	Wall Shear Stress Patterns . . . . .	36
6.2.3	Spectral Analysis . . . . .	39
<b>7</b>	<b>Wall-Model for Charles<sup>X</sup></b>	<b>46</b>
7.1	Current Inner Layer Wall-Model . . . . .	46
7.2	Rotation Corrected Wall-Model . . . . .	47
7.3	Stand-Alone Wall-Model Algorithm . . . . .	48
7.4	<i>A Priori</i> Testing Methodology . . . . .	51
7.5	<i>A Priori</i> Testing Results . . . . .	51
7.5.1	Mean Quantities . . . . .	51
7.5.2	Instantaneous Statistics . . . . .	54
<b>8</b>	<b>Wall-Modeled Large Eddy Simulation</b>	<b>57</b>
8.1	Setup . . . . .	57
8.2	Results . . . . .	58
<b>9</b>	<b>Conclusions and Future Work</b>	<b>64</b>

# Symbols and abbreviations

## English Symbols

$A^+$	van Driest damping constant
$B$	log-law constant term
$C_v$	specific heat in constant volume
$C_p$	specific heat in constant pressure
$C_{DES}$	Detached Eddy Simulation constant
$\mathcal{C}_{ij}$	Coriolis Reynolds Stress
$\tilde{d}$	DES Spalart-Almaras turbulence model trigger
$E$	total Energy, turbulence kinetic energy
$F$	volume Flux
$f$	flux density
$G$	LES filter kernel
$D$	van Driest damping function
$h$	half-channel height
$k$	wavenumber
$L$	characteristic length, domain dimension
$l$	mixing length
$N$	cell index
$\vec{n}$	normal vector
$\mathcal{P}_{ij}$	Reynolds stress shear production
$p$	pressure
$Pr$	Prandtl number
$Q_j$	SGS temperature flux ( $C_p Q_j$ SGS heat flux)
$q_j$	heat flux
$R$	specific gas constant, Correlation Coefficient
$Re$	Reynolds number
$Ro$	rotation number (inverse Rossby number)
$Ri$	gradient Richardson number
$\vec{R}$	arbitrary position vector in inertial coordinates
$\vec{r}$	arbitrary position vector in rotating coordinates
$S$	cell face area, Bradshaw's parameter
$S_{ij}$	strain rate tensor
$T$	temperature
$t$	time
$u$	velocity vector component in $x$ -direction
$v$	velocity vector component in $y$ -direction
$V$	cell volume
$w$	velocity vector component in $z$ -direction

## Greek Symbols

$\alpha_{ij}$	Vreman model coefficient tensor
$\alpha$	rotation correction coefficient exponent
$\beta$	rotation correction coefficient constant
$\gamma$	specific heat ratio
$\delta_{ij}$	Kronecker's delta
$\Delta$	filterwidth
$\Delta_s$	displacement
$\epsilon_{ijk}$	Levi-Civita tensor
$\epsilon_{ij}$	Reynolds stress dissipation
$\kappa$	von Kármán constant
$\mu$	dynamic viscosity
$\nu$	kinematic viscosity
$\Pi_{ij}$	Reynolds stress pressure-strain
$\rho$	density
$\sigma_{ij}$	total stress tensor
$\tau_{ij}$	sub-grid scale stress tensor
$\tau_w$	wall shear stress
$\phi$	generalized flow variable
$\psi$	generalized flow variable
$\vec{\Omega}$	angular velocity vector

## Subscripts, Superscripts & Brackets

+	wall unit
^	Fourier transformed
'	fluctuating component (results and RANS context), small scale quantity (LES filtering context)
-	time-averaged quantity (results and RANS context), filtered quantity (LES and WM context)
~	Favre-filtered
$w$	wall
$wm$	wall-model
	wall-parallel
$m$	mean
$n$	normal
$p$	pressure side
$s$	suction side
$SGS$	sub-grid scale
$b$	bulk
$t$	turbulent, eddy
$c, crit$	critical

$\langle \rangle$  averaging in homogeneous direction or plane

## Operators

$\vec{a} \cdot \vec{b} = \sum_{i=1}^n a_i b_i$	dot product of two vectors
$\vec{a} \times \vec{b} = \begin{vmatrix} \vec{i} & \vec{j} & \vec{k} \\ a_1 & a_2 & a_3 \\ b_1 & b_2 & b_3 \end{vmatrix}$	cross product of two vectors
$\nabla = \frac{\partial}{\partial x} \vec{i} + \frac{\partial}{\partial y} \vec{j} + \frac{\partial}{\partial z} \vec{k}$	del operator
$\nabla \phi = \frac{\partial \phi}{\partial x} \vec{i} + \frac{\partial \phi}{\partial y} \vec{j} + \frac{\partial \phi}{\partial z} \vec{k}$	gradient of a scalar field
$\nabla \cdot \vec{a} = \frac{\partial a_1}{\partial x} + \frac{\partial a_2}{\partial y} + \frac{\partial a_3}{\partial z}$	divergence of a vector field
$\nabla \times \vec{a} = \begin{vmatrix} \vec{i} & \vec{j} & \vec{k} \\ \frac{\partial}{\partial x} & \frac{\partial}{\partial y} & \frac{\partial}{\partial z} \\ a_1 & a_2 & a_3 \end{vmatrix}$	curl of a vector field
$(f * g)(x) = \int_{-\infty}^{\infty} f(x - \xi) g(\xi) d\xi$	convolution of two functions

## Abbreviations

BC	Boundary Condition
CFD	Computational Fluid Dynamics
DDES	Delayed Detached Eddy Simulation
DES	Detached Eddy Simulation
DNS	Direct Numerical Simulation
EL	Exchange Location (wall-model)
FDM	Finite Difference Method
FEM	Finite Element Method
FVM	Finite Volume Method
IDDES	Improved Delayed Detached Eddy Simulation
LES	Large Eddy Simulation
RANS	Reynolds Averaged Navier-Stokes
SGS	Sub-grid Scale
TBLE	Thin Boundary Layer Equations
URANS	Unsteady Navier-Stokes
WMLES	Wall-Modeled Large Eddy Simulation

# 1 Introduction

Rotating flows are common phenomena in engineering applications as well as in nature. Turbomachinery, ocean currents, hurricanes and even spiral galaxies are few examples of the vast variety of applications that are affected by system rotation. Rotating flows are commonly investigated in a rotating reference frame, in which the observer rotates with the system. In fact, the surface of the earth itself is a rotating reference frame, and the Large Eddy Simulation method was originally developed in order to study atmospheric flows [3].

Transforming the equations of motion from an inertial frame into a rotating frame introduces two additional fictitious accelerations: the Coriolis acceleration and the centrifugal acceleration. These fictitious forces have major effects in general flow behavior and turbulence. They are the reason why storms start to swirl and form hurricanes on the Earth's surface, and why the turbulent activity between two blades of a radial pump is increased on one blade and decreased on the other. [4]

Due to general development in computational resources, Computational Fluid Dynamics (CFD) has become an important toolkit for engineers and researchers working on fluid mechanics. Its beauty lies in its almost endless possibilities varying from fundamental turbulence research to preliminary design optimization in engineering applications. The numerical models, which in reality are only zeros and ones in a computer's memory, provide a possibility to design and optimize products as well as to study natural phenomena without the major expenses of experimental testing.

## 1.1 Simulating Turbulent Flows: Level of Approximation

Turbulence is a very common phenomenon that is encountered in almost every moving fluid and rotating flows are no exception. Sir Osbourne Reynolds (1883) introduced a dimensionless quantity from which we can deduce whether a flow is turbulent or not. This dimensionless Reynolds number describes the ratio of inertial and viscous forces, and mathematically it can be expressed as

$$Re = \frac{\rho U_m L}{\mu} , \quad (1)$$

where  $\rho$  is the fluid density,  $U_m$  is the relative mean velocity of the fluid,  $L$  is a characteristic dimension, and  $\mu$  is the dynamic viscosity of the fluid. Several experiments over the years have showed that flows undergo a transition from laminar to turbulent when inertial forces become dominant over viscous forces, and a case specific critical Reynolds number is used to describe this transition point. The critical Reynolds number varies between different simulation setups, since the characteristic length needs to be chosen adequately.

The significance of rotation effects are typically expressed with a similar dimensionless parameter called the Rossby number. In this thesis, we adapt to the general notation found in the context of rotating shear flows and define the rotation with

the inverse Rossby number, which is referred to as the rotation number. It is defined as the ratio of the velocity associated with rotation and the mean fluid velocity

$$Ro = \frac{2|\vec{\Omega}|L}{U_m}, \quad (2)$$

where  $|\vec{\Omega}|$  is the magnitude of the angular velocity vector. Using these two dimensionless quantities, a rotating flow setup can be explicitly defined and they will be referred to throughout the thesis.

Although the presence of turbulence can be easily observed and even calculated through Reynolds number, giving an absolute definition for it is a difficult task. Hinze (1959) [5] defined turbulence as an irregular condition of a flow where quantities vary randomly in time and space coordinates. He also noted that it is possible to distinguish average values in varying quantities, which can be analyzed since they are not sensitive to initial conditions. The structure of turbulence consists of a range of eddies or whirls with different length scales. These eddies contain energy, which is transferred in a process referred to as the energy cascade. In this process, large eddies absorb kinetic energy from the mean flow and pass it to smaller scales through various interactions. Finally, the turbulent kinetic energy is dissipated through the smallest scales, the Kolmogorov scales, by viscous effects.

The basis for all fluid dynamics modeling is the numerical solution of the Navier-Stokes equations. In the simulation process, the investigated flow domain is divided into cells or elements that are used to calculate a discrete solution. Different approaches to calculate the flow field have been proposed, the most common being the Finite Volume Method (FVM), which relies on the expression of fluxes to calculate the partial derivatives in discrete volumes (cells). Another approach is the Finite Difference Method (FDM) which calculates the partial derivatives directly through difference schemes that can be derived from the Taylor series. The third main approach is the Finite Element Method (FEM) and its variants which have become increasingly popular in the academia. Their principle is to express the solution with piecewise polynomials to calculate the solution with higher precision than linear expressions resulting from FVM and FDM.

Finding an efficient way to include the effects of turbulence into the solution has been found to be the most problematic aspect of CFD, and various approaches have been proposed. The approach that resolves the entire turbulence energy spectrum is resolved without any averaging is called Direct Numerical Simulation (DNS). However, according to the Kolmogorov's theory, the requirement for the number of grid points to resolve all scales of turbulence in a cubic volume is proportional to  $Re^{9/4}$ , making DNS at high Reynolds numbers impossible even for current supercomputers [6]. Since resolving all turbulence scales is rarely feasible, compromises have to be made by introducing averaging to the governing equations.

In the classical RANS method, a time averaged solution is calculated by solving Reynolds Averaged Navier-Stokes equations. In this method, none of the turbulence scales are resolved and the effects of turbulence are taken into account entirely by turbulence modeling. The principle task of turbulence models is to transport the information of turbulence quantities, such as turbulent kinetic energy and dissipa-

tion. Based on the local values of these parameters, the steady flow field is then modified by adding artificial eddy viscosity to reflect the increase in diffusion due to turbulence. RANS method is widely used, and several different turbulence models have been proposed. It is primarily applicable for steady-state flows where the unsteady flow structures have a minor role in the analysis.

The Large Eddy Simulation (LES) can be considered to be in between the two extremities, DNS and RANS. In LES, large turbulence scales are resolved and small scales are modeled. Ideally, LES can be considerably more inexpensive in terms of computational requirements than DNS, since only the dynamically important motions resulting from the flow configuration need to be resolved. However, applying LES to turbulent boundary layers changes LES to be significantly more demanding, since the dynamically important scales of the inner boundary layer (10-20% of the boundary layer) tend to decrease as a function of Reynolds number. According to Chapman's landmark paper [6] published in 1979, the required number of grid points is proportional to  $Re^{9/5}$  if the inner layer is resolved which causes LES to be almost as expensive as DNS in terms of computational requirements. However, this very strict inner-layer requirement can be bypassed by using approximative near-wall treatments, and Chapman gave an estimate that the grid point requirement reduces to be proportional to  $Re^{2/5}$  when the inner layer is modeled.

The fundamental idea for wall-modeling in LES is to evaluate the wall shear stress in a simplified process and use it as a boundary condition. Several near-wall treatments can be found in the literature and they can be divided into two main groups: Wall-stress models and RANS/LES hybrids. The wall-stress models are weakly coupled to the LES calculation and model the wall shear stress directly from the LES quantities. In this thesis, we further divide them into two sub-classes which are the approximative boundary conditions and the auxiliary grid models. The approximative boundary conditions modify the boundary conditions to fulfill a generalized law at the first off-wall cells, while the auxiliary grid models calculate the inner boundary layer with a simplified set of equations in an embedded auxiliary grid. The RANS/LES hybrids are strongly coupled wall treatments which do not directly model the wall shear stress. They utilize a single grid and switch to RANS simulation near the wall, from which the wall shear stress can be calculated. [7]

Several levels of approximations can be made in order to reduce the computational requirements. On the other hand, these approximations naturally distort the real physics and therefore affect the accuracy of the results. In addition, flow characteristics also limit the approximations, as the steady-state RANS is unable to capture highly unsteady flow phenomena. Thus, the suitable level of approximation needs to be set accordingly to satisfy the complexity of the flow and as a compromise between the desired accuracy and computational requirements.

## 1.2 Previous Research

A spanwise rotating turbulent channel flow is a convenient test case in order to study the effects of system rotation. The first experimental studies to investigate these effects were performed by Hill & Moon(1962) [8], Moon (1964) [9] and Moore

(1967) [10]. In 1969, Bradshaw extensively studied the stability effects of wall curvature and system rotation. In his landmark paper [11], he introduced a stability parameter called the gradient Richardson number, which locally describes whether the turbulent activity is enhanced or diminished. Conceivably, the most conductive experiments on the rotating turbulent channel were performed by Johnston, Alleen and Lezius in 1973 [12]. They demonstrated the role of Bradshaw's stability parameters and gave detailed descriptions of the physical flow phenomena behind these stability effects, which will be discussed in Chapter 4.

Large Eddy Simulations of a spanwise rotating channel were carried out by Kim(1983) [13] and Miyake & Kajishima(1986) [14]. They observed similar flow structures as Johnston et al. had previously presented. Further numerical studies were done by Kristoffersen & Andersson (1993)[1], Lamballais et al. (1996)[15] and Alvelius (1999) [16] as they performed DNS with relatively low Reynolds numbers, but with a wide range of rotation rates. More recently, Wallin et al.(2013) [17] investigated the laminarization mechanisms at very high Rotation numbers. They observed that Tollmien-Schlichting type of plane waves are unaffected by the system rotation, and they can cause periodic bursting events when the flow is about to laminarize.

Near-wall treatments for the Large Eddy Simulation have been studied since 1970s. The first wall modeling approach was proposed by Deardorff (1970) [18] in which he assumed isotropic turbulence near the wall and enforced the velocities to satisfy the logarithmic law by defining the second derivatives at the first off-wall gridpoint. The wall-model by Schumann (1975) [19] was the first true wall-stress model based on the assumption of the wall shear stress being proportional to the near-wall velocity. Grötzbach (1987) [20] later improved this model by removing the requirement of *a priori* known wall shear stress to make it feasible as a predictive method. In 1996, Balaras et al. [21] published the first auxiliary grid model that utilizes the thin boundary layer equations (TBLE) and they also applied it to a rotating channel. The authors found the results to be in relatively good agreement with the DNS data in cases of low rotation rates, but due to the logarithmic velocity profile assumption, the results became worse when the rotation was increased.

More recently, several variations of existing wall-models have been developed and proposed. For example, Wang and Moin (2002) [22] proposed a dynamic coefficient for the mixing length model used in the TBLE model. The more recent approaches also include different variations of RANS/LES hybrids, the first proposal being the Detached Eddy Simulation (DES) with an adaptive SGS-Spalart-Allmaras turbulence model by Spalart et al. (1997) [23]. Another renowned DES approach based on extended SST  $k-\omega$  turbulence model was published by Strelets [24] in 2001, which targets massively separated flows. Lately, especially the near-wall treatment capabilities of DES have been improved, resulting in approaches, such as Delayed Detached Eddy Simulation (DDES) and Improved Delayed Detached Eddy simulation (IDDES). Although the near-wall treatment is very highly researched topic, wall-modeling for Large Eddy Simulations of rotating flows specifically is still a relatively unexplored field due to the complex stability phenomena resulting from the Coriolis effect.

### 1.3 Present Research Objectives

The first primary objective in this thesis is to study near-wall treatment approaches for LES in general. After the short literature review, we will focus on the Charles<sup>X</sup> DNS/LES solver available at the department and implement the additional source terms resulting from the rotating frame transformation. In addition, a test case will be performed to validate the solver and the additional source terms. The third primary objective is to perform high Reynolds number simulations to obtain reference data for *a priori* wall-model testing. The current wall-model found in Charles<sup>X</sup> is then implemented into a stand-alone python program and its behavior is analyzed by applying it to the wall-resolved results. In addition, the feasibility of the *a priori* testing will be investigated by studying the instantaneous statistics. Based on these *a priori* results, a wall-model correction will be proposed, and the improvements are implemented into the solver as well as tested by performing Wall-Modeled Large Eddy Simulations (WMLES).

## 2 Large Eddy Simulation Principles

The principles of the Large Eddy Simulation were published in 1963 by Smagorinsky [3]. The main objective in the development of these equations was the excessive requirements of resolving all scales, which Kolmogorov had previously discussed. Kolmogorov had also identified that the smallest turbulence motions are mainly isotropic and could be considered as homogeneous. This information combined with the general principle of the energy cascade, which states that the smallest scales are not as dependent on the boundary conditions as they mainly act as an energy sink, lead to the idea of approximately modeling these small homogeneous scales. On the contrary, the more energetic large scales, which do most of the energy transportation from the core flow, and thus are greatly affected by boundary conditions, should be directly resolved. This decomposition of the turbulence energy spectrum into resolved large scales and modeled small scales is the main principle of Large Eddy Simulation and it is illustrated in Figure 1. [25]

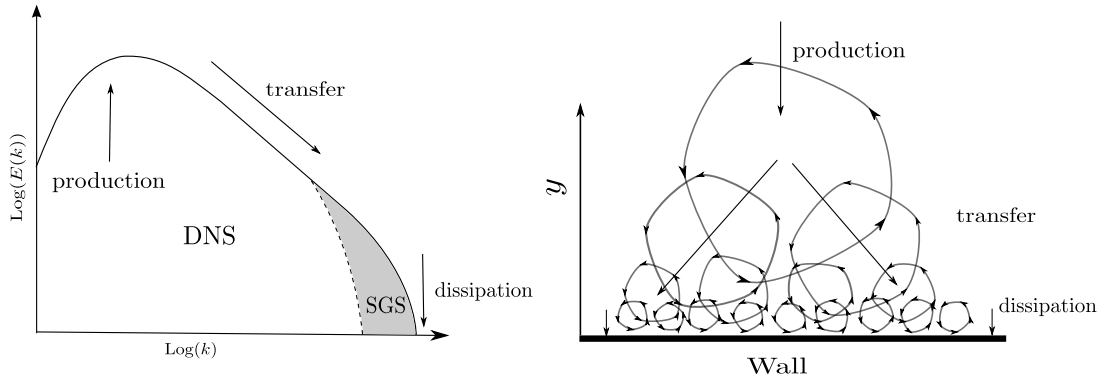


Figure 1: The energy spectrum decomposition and corresponding energy cascade principle.

### 2.1 Scale Decomposition

The scale decomposition is done by introducing spatial averaging to the Navier-Stokes equations, which is typically referred to as filtering. The decomposition into the resolved and modeled quantities can be expressed as

$$\phi(\vec{x}, t) = \bar{\phi}(\vec{x}, t) + \phi'(\vec{x}, t) , \quad (3)$$

where the overbar denotes the resolved large scales and the prime modeled small scales. Algebraically, the filter operation can be written as a convolution of the filter kernel and the filtered quantity

$$\bar{\phi}(\vec{x}, t) = \int_D G(\vec{x} - \vec{\xi}) \phi(\vec{\xi}, t) d\vec{\xi} , \quad (4)$$

where  $\vec{\xi}$  is the integration dummy variable and  $D$  is the flow domain. Sagaut [26] specifies three criteria that a filter operator should fulfill: Firstly, the filter operation

should conserve constants,

$$\bar{a} = a \iff \int_D G(\vec{x} - \vec{\xi}) d\vec{\xi} = 1 . \quad (5)$$

Secondly, the filtered quantities should conserve linearity,

$$\overline{\phi + \psi} = \bar{\phi} + \bar{\psi} . \quad (6)$$

Thirdly, the commutation with differentiation should be exact,

$$\frac{\partial \bar{\phi}}{\partial s} = \frac{\partial \bar{\phi}}{\partial s} , \quad s = \vec{x}, t . \quad (7)$$

However, the direct commutation of quantities does not hold

$$\overline{\phi\psi} \neq \bar{\phi}\bar{\psi} . \quad (8)$$

This leads to a commutation error, which in fact is the subgrid-scale term to be modeled

$$\overline{\phi\psi} = \bar{\phi}\bar{\psi} + \tau = \bar{\phi}\bar{\psi} + (\overline{\phi\psi} - \bar{\phi}\bar{\psi}) , \quad (9)$$

where  $\tau$  denotes the commutation error. In addition, the commutation error is typically further decomposed by combining the terms describing similar scale interactions. By substituting  $\phi = \bar{\phi} + \phi'$  and  $\psi = \bar{\psi} + \psi'$  into the expression of  $\tau$  in Equation (9), the decomposed form of the commutation error becomes

$$\tau = \overline{(\bar{\phi} + \phi')(\bar{\psi} + \psi')} - \bar{\phi}\bar{\psi} = (\overline{\bar{\phi}\bar{\psi}} - \bar{\phi}\bar{\psi}) + (\overline{\bar{\phi}\psi'} + \overline{\bar{\psi}\phi'}) + (\overline{\phi'\psi'}) . \quad (10)$$

The first bracketed term on the right-hand side in Equation (10) is the Leonard term, which represents the production of subgrid turbulence by the large resolved eddies. The second term is the cross-stress term, which represents the interactions between the large resolved scales and the small modeled scales. The final term is the Reynolds term and it describes only the interactions within the small modeled turbulence scales, and therefore it is occasionally called the sub-grid scale Reynolds stress.

Since the solver utilized in this project is implemented with the FVM, the filter kernel is not explicitly defined. However, the filter kernel can be considered as a physical space box filter in which the grid works as the filter. The box filter can be expressed as

$$G(\vec{x} - \vec{\xi}) = \begin{cases} 1/\bar{\Delta} & \text{if } |\vec{x} - \vec{\xi}| \leq \frac{\bar{\Delta}}{2} \\ 0 & \text{otherwise} \end{cases} , \quad (11)$$

where  $\bar{\Delta}$  is the cut-off length. Simply put, in the Finite Volume Method, the filter is the grid itself and the cell values represent the spatial average inside the cells. Thus, in the Finite Volume Method, it is impossible to resolve turbulent scales which are shorter than the distance between the centers of two adjacent cells.

Since Charles<sup>X</sup> is a compressible solver, Favre filtering is also introduced to the flow quantities. The Favre filtering is a name for a change of variables, where the solution variables are weighted by density, and it is defined as

$$\overline{\rho\phi} = \bar{\rho}\tilde{\phi} . \quad (12)$$

The Favre filtering is done in order to avoid extra subgrid-scale that result from the decomposition of terms such as,  $\overline{\rho u_i}$  to  $\bar{\rho}\tilde{u}_i$ . [27]

## 2.2 Navier-Stokes Equations

The Navier-Stokes equations are presented in the Eulerian conservation form, meaning that the change in flow quantities are examined in a differential stationary frame rather than following individual fluid particles. The first Navier-Stokes equation is the continuity equation that defines the conservation of mass in this frame. The second equation is the momentum equation, which practically is the Newton's second law  $F = ma$  for a continuum. The left-hand side in this equation represents the accelerations, while the terms on the right-hand side are the surface forces of the control volume. The final equation is the energy equation, defining the conservation of energy. Several formulations for the energy equation can be found in the literature, and in this thesis the formulation for the total energy is used as it is also implemented in the utilized solver. The full group of Navier-Stokes equations for a compressible fluid is given by

$$\frac{\partial \rho}{\partial t} + \frac{\partial \rho u_j}{\partial x_j} = 0 , \quad (13)$$

$$\frac{\partial \rho u_i}{\partial t} + \frac{\partial \rho u_i u_j}{\partial x_j} = -\frac{\partial p}{\partial x_i} + \frac{\partial \sigma_{ij}}{\partial x_j} , \quad (14)$$

$$\frac{\partial(\rho E)}{\partial t} + \frac{\partial(\rho E + p)u_j}{\partial x_j} = \frac{\partial(u_{ij}\sigma_{ij})}{\partial x_j} - \frac{\partial q_j}{\partial x_j} , \quad (15)$$

where  $t$  denotes time,  $E$  is the total energy per mass unit and  $p$  is the pressure. The tensor notations  $x_i$  and  $u_i$  represent the cartesian spatial coordinate vector and the velocity vector respectively. The sub-indices  $i$  and  $j$  vary from 1 to 3, denoting the three components of the velocity vector  $u, v, w$  and the coordinate vector  $x, y, z$ . The term  $\sigma_{ij}$  is the total stress tensor that comprises of a total of nine components and it is defined as

$$\sigma_{ij} = 2\mu(T)S_{ij} - \frac{2}{3}\mu(T)\delta_{ij}S_{kk} , \quad (16)$$

where  $\delta$  is the Kronecker delta, which is valued 0 if  $i \neq j$  and 1 if  $i = j$ . The strain rate tensor  $S_{ij}$  is given by

$$S_{ij} = \frac{1}{2} \left( \frac{\partial u_j}{\partial x_i} + \frac{\partial u_i}{\partial x_j} \right) . \quad (17)$$

In the energy equation, the total energy per mass unit  $E$  for a perfect gas is defined as

$$\rho E = \frac{p}{\gamma - 1} + \frac{1}{2} \rho u_i u_i , \quad (18)$$

$$\gamma = \frac{C_p}{C_v} , \quad (19)$$

where  $C_p$  and  $C_v$  are the specific heat capacities at constant pressure and constant volume. The density and the pressure are coupled to the temperature  $T$  by the equation of state

$$p = \rho R T , \quad (20)$$

in which

$$R = C_p - C_v . \quad (21)$$

Furthermore, the dynamic viscosity can be linked to the temperature via the power law

$$\frac{\mu}{\mu(T_0)} = \left( \frac{T}{T_0} \right)^{0.76} , \quad (22)$$

which is valid from 150 K to 500 K. The heat flux  $q_j$  is defined as

$$q_j = -\kappa \frac{\partial T}{\partial x_j} , \quad (23)$$

in which  $\kappa$  is the thermal conductivity that can be expressed as

$$\kappa = \mu C_p / Pr . \quad (24)$$

In the expression of thermal conductivity,  $Pr$  is the Prandtl number. It represents the ratio of the kinematic viscosity and the thermal diffusivity and is typically assumed to be constant  $Pr = 0.72$ . [27]

## 2.3 Filtered Governing Equations

As a result from the previously introduced Favre filtering, applying the filter operator to the continuity equation is straightforward and the filtered continuity equation is simply expressed as

$$\frac{\partial \bar{\rho}}{\partial t} + \frac{\partial (\bar{\rho} \tilde{u}_i)}{\partial x_i} = 0 . \quad (25)$$

In the momentum equation, the filtered convective terms need to be decomposed as

$$\overline{\rho u_i u_j} = \bar{\rho} \widetilde{u_i u_j} + \tau_{ij} , \quad (26)$$

which results in the following sub-grid scale stress tensor to be modeled

$$\tau_{ij} = \bar{\rho} (\widetilde{u_i u_j} - \tilde{u}_i \tilde{u}_j) . \quad (27)$$

Thus, the resulting filtered momentum equation can be written as

$$\frac{\partial(\bar{\rho}\tilde{u}_i)}{\partial t} + \frac{\partial(\bar{\rho}\tilde{u}_i\tilde{u}_j)}{\partial x_j} = -\frac{\partial\bar{p}}{\partial x_i} + \frac{\partial\tilde{\sigma}_{ij}}{\partial x_j} - \frac{\partial\tau_{ij}}{\partial x_j}, \quad (28)$$

where the filtered total stress tensor is

$$\tilde{\sigma}_{ij} = 2\mu(\tilde{T})\tilde{S} - \frac{2}{3}\mu(\tilde{T})\delta_{ij}\tilde{S}_{kk}. \quad (29)$$

The filtered strain-rate tensor can be simply written with the filtered velocities as

$$\tilde{S}_{ij} = \frac{1}{2} \left( \frac{\partial\tilde{u}_i}{\partial x_j} + \frac{\partial\tilde{u}_j}{\partial x_i} \right). \quad (30)$$

Applying the filter operator to the energy equation is more complex, and several different variations and simplified forms can be found in the literature. In the total energy formulation, the filtered total energy is defined as

$$\bar{\rho}\tilde{E} = \frac{\bar{p}}{\gamma - 1} + \frac{1}{2}\widetilde{\rho u_i u_i}, \quad (31)$$

where the Favre filtered term needs to be further decomposed as

$$\bar{\rho}\tilde{E} = \frac{\bar{p}}{\gamma - 1} + \frac{1}{2}\bar{\rho}\tilde{u}_i\tilde{u}_i + \frac{\tau_{ii}}{2}. \quad (32)$$

In the equation above,  $\tau_{ii}$  represents the SGS kinetic energy. This expression together with the Favre filtered equation of state  $\bar{p} = \bar{\rho}R\tilde{T}$  gives the coupling between filtered pressure, density and temperature. Introducing the filter operator to all terms in the energy equation, the following form is obtained

$$\begin{aligned} \frac{\partial(\bar{\rho}\tilde{E})}{\partial t} + \frac{(\bar{\rho}\tilde{E} + \bar{p})\tilde{u}_j}{x_j} - \frac{\partial(\tilde{u}_{ij}\tilde{\sigma}_{ij})}{\partial x_j} + \frac{\partial\tilde{q}_j}{\partial x_j} = \\ - \frac{\partial}{\partial x_j} [(\overline{\rho u_j E} - \bar{\rho}\tilde{u}_j\tilde{E}) + (\overline{u_j p} - \tilde{u}_j\bar{p}) + (\overline{\sigma_{ij}u_j} - \tilde{\sigma}_{ij}\tilde{u}_j) - (\bar{q}_j - \tilde{q}_j)], \end{aligned} \quad (33)$$

where the entire right-hand side ideally needs to be SGS modeled. The first two terms on the right-hand side can be joined together by using the expression in Equation (32), which gives

$$\begin{aligned} \frac{\partial(\bar{\rho}\tilde{E})}{\partial t} + \frac{(\bar{\rho}\tilde{E} + \bar{p})\tilde{u}_j}{x_j} - \frac{\partial(\tilde{u}_{ij}\tilde{\sigma}_{ij})}{\partial x_j} + \frac{\partial\tilde{q}_j}{\partial x_j} = \\ - \frac{\partial}{\partial x_j} [C_p Q_j + J_j + D_j - (\bar{q}_j - \tilde{q}_j)], \end{aligned} \quad (34)$$

where

$$C_p Q_j = C_p \bar{\rho}(\widetilde{u_j T} - \tilde{u}_j \tilde{T}) \quad (35)$$

is the SGS heat flux,

$$J_j = \frac{1}{2}(\widetilde{\bar{\rho}u_j u_i u_i} - \bar{\rho}\tilde{u}_j\tilde{u}_i\tilde{u}_i - \tau_{ii}) \quad (36)$$

is the SGS turbulent diffusion,

$$D_j = \overline{\sigma_{ij}u_j} - \tilde{\sigma}_{ij}\tilde{u}_{ij} \quad (37)$$

is the SGS viscous diffusion. The final term  $(\bar{q}_j - \tilde{q}_j)$  is an additional SGS heat flux term resulting from the non-linearity of the viscosity-temperature coupling. Several studies, such as the one by Meng & Pletcher [28], have found the SGS heat flux  $C_p Q_j$  to have the most impact on the results and the rest to be negligible. Same approach is also adapted in the SGS model found in the Charles<sup>X</sup> solver. [27]

## 2.4 Subgrid-Scale Modeling

As mentioned earlier, subgrid-scale models are used in LES to model the effects of smaller scales, which can not be resolved by the grid. The most widely used SGS models are eddy viscosity models, which are based on the Boussinesq hypothesis. The hypothesis states that the effects of homogeneous turbulence can be described with an artificial eddy viscosity, reflecting the increase in dissipation due to turbulence. The Boussinesq hypothesis is defined as

$$\tau_{ij}^d = \tau_{ij} - \frac{1}{3}\tau_{kk}\delta_{ij} = -2\mu_{SGS} \left( \tilde{S}_{ij} - \frac{1}{3}\delta_{ij}\tilde{S}_{kk} \right) . \quad (38)$$

The first and still very popular SGS model, that is known for its robustness, is the Smagorinsky model. It has been the basis for the more advanced models, which can be considered as variants of it. The eddy viscosity in the Smagorinsky SGS model is defined as

$$\mu_{SGS} = \rho(C_s\Delta)^2|\tilde{S}| , \quad (39)$$

where  $\Delta$  is the filter width, typically  $\Delta = V_{cell}^{\frac{1}{3}}$ ,  $|\tilde{S}| = \sqrt{2\tilde{S}_{ij}\tilde{S}_{ij}}$ , and  $C_s$  is an empirical Smagorinsky constant  $C_s = 0.1 - 0.2$ . As seen from the equations above, the Smagorinsky SGS approach is very straightforward and only requires the information of the local cell size as well as the first velocity derivatives. [27]

### 2.4.1 Vreman Model

Simple eddy viscosity models, such as Smagorinsky model, do not function properly in transitional and laminar regions, since there is no feature to limit the eddy viscosity within these areas. The Vreman SGS model [29] is a more advanced and dynamic approach to provide this support. The feasibility in transitional regions is a highly desirable feature especially for rotating flows, since the system rotation greatly affects the local stability and can locally laminarize the flow [12].

The Vreman model modifies the expression of the eddy viscosity to be

$$\mu_{SGS} = \rho C_{vr} \sqrt{\frac{B_\beta}{\alpha_{ij}\alpha_{ij}}} , \quad (40)$$

where the dynamic parameters are defined as

$$\alpha_{ij} = \frac{\partial \bar{u}_j}{\partial x_i} , \quad (41)$$

$$\beta_{ij} = \Delta_m^2 \alpha_{mi} \alpha_{mj} , \quad (42)$$

$$B_\beta = \beta_{11}\beta_{22} - \beta_{12}^2 + \beta_{11}\beta_{33} - \beta_{13}^2 + \beta_{22}\beta_{33} - \beta_{23}^2 . \quad (43)$$

The model constant  $C_{vr}$  is defined as  $c \approx 2.5C_s^2$ . Although the Vreman model contains several different dynamic parameters, they also depend only on the filter width and the first velocity derivatives. Therefore, the implementation of the model is not drastically more complex than the Smagorinsky model and it has been found to be robust as well.

#### 2.4.2 SGS Heat Flux

Regardless of the energy equation formulation, the SGS heat flux needs to be calculated. The majority of authors utilize the gradient hypothesis by Eidson [30], which states that the energy transfer resulting from small scales is proportional to the resolved temperature gradient. Furthermore, the Charles<sup>X</sup> solver applies the strong Reynolds analogy by Morkovin (in Hadjadj et al. [31]) to calculate the SGS heat flux. According to Morkovin hypothesis, the analogy between the momentum and heat flux is independent on Mach number for non-supersonic flows, which essentially leads to the expression

$$C_p Q_j = -C_p \frac{\mu_{SGS}}{Pr_{SGS}} \frac{\partial \tilde{T}}{\partial x_j} , \quad (44)$$

where  $Pr_{SGS}$  is the sub-grid scale Prandtl number which relates the SGS eddy viscosity to the SGS thermal diffusivity. Several experiments and numerical studies have proved that using a constant value  $Pr_{SGS} = 0.9$  is sufficient for non-supersonic flows and this value is also used in this project [27].

### 3 Near-Wall Treatment Approaches for LES

#### 3.1 Motivation for Wall-Modeling

The turbulent boundary layer can be divided into two separate layers, the inner and the outer layer. The layer separation is associated with different governing time and length scales in the immediate vicinity of the wall and in the core flow. This behavior causes LES to have different grid resolution requirements for both layers. The requirement for the outer layer is based on providing a sufficient resolution to capture the most meaningful turbulence dynamics resulting from the flow configuration, which are typically few percentages of the largest length scale. On the contrary, the resolution requirement for the inner layer results from capturing the notably smaller turbulence scales, which are highly proportional to Reynolds number. Choi & Moin [32] derived even slightly higher Reynolds number dependency for the grid requirement than Chapman had previously introduced. According to them, the Reynolds number dependencies for the outer and inner layer are respectively

$$N_{xyz} \sim Re_{L_x}^{0.28} \text{ (outer layer) ,} \quad (45)$$

$$N_{xyz} \sim Re_{L_x}^{1.85} \text{ (inner layer) .} \quad (46)$$

Figure 2 shows the total grid point requirement for a turbulent boundary layer over a flat plate with an aspect ration of 4, calculated with the methodology by Choi & Moin. This graph encapsulates the necessity of wall-modeling at high Reynolds numbers. For example, in a hypothetical case of simulating an entire aircraft with  $Re = 10^8$ , the simulation would require placing 99% of all cells within the inner boundary layer, although it covers only a small fraction of the entire computational domain.

Experimental and numerical studies have showed that the turbulence behavior in the outer layer is highly affected by the flow configuration i.e. boundary conditions, while inner layer is constant in wall units [7]. This favorable behavior can be seen in the illustrative visualization of the spectral densities of turbulent kinetic energy by Jimenez [33] in Figure 3. The visualization shows that the most energetic turbulence length scales  $\lambda_x^+$  are nearly constant up to  $y^+ = 80$  (inner layer) , after which they start to grow linearly in a logarithmic scale. This ‘universal’ behavior in wall units provides a baseline to bypass the strict inner layer requirements via wall-modeling, while using the predicting capabilities of LES to simulate the outer layer. However, wall-modeled simulations do not target producing cheaper low Reynolds number simulations, since the outer layer requirement cannot be avoided. The main goal for wall-modeling rather is to extend the range of feasible high Reynolds number simulations.

Several different near-wall treatments have been proposed for LES over the past 40 years. Previous wall-model reviews have classified these models into different groups based on their modeling approach. However, the division of the wall-models varies between different studies and different terms are being used to describe the approaches. In this short literature review, the approaches are divided into two

separate classes: the wall-stress models and the RANS/LES hybrids. The wall-stress models are further classified into two subclasses, which are the approximative boundary conditions and the auxiliary grid models. In the following chapters, the principles of each approach will be introduced and corresponding milestone wall-models will be shortly discussed.

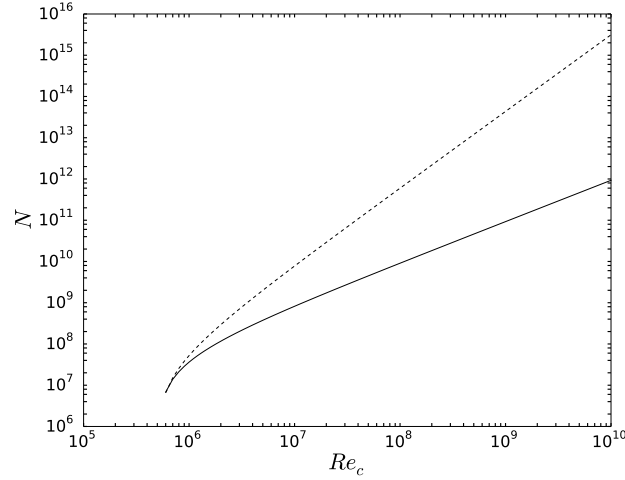


Figure 2: Grid point requirement for a turbulent boundary layer over a flat plate.

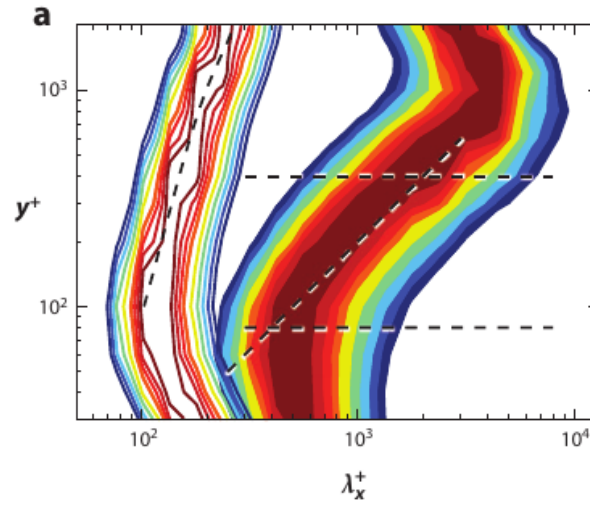


Figure 3: Right curve: Highest 14 % of the spectral density of  $kE$  in wall-bounded turbulence [33].

### 3.2 Wall-Stress Models

The first wall-model proposals are all based on the equilibrium assumption that the velocities at the first off-wall grid point at  $30 < y^+ < 300$  satisfy the logarithmic velocity profile, also known as the law of the wall. These models link the velocity

at the first off-wall grid point to the wall shear stress through a modified boundary condition and can be considered to be similar as wall functions in RANS framework. Moreover, the shear stress is assumed to be constant in the whole inner layer and in the simplest approaches, direct viscous effects are even neglected. The standard expression for the logarithmic velocity profile is

$$u^+ = \frac{1}{\kappa} \ln y^+ + B , \quad (47)$$

where  $\kappa$  is the von Kármán constant which is typically  $\kappa = 0.41$  and  $B$  is a constant  $B \approx 5.0 - 5.5$ . The wall units are defined as  $y^+ = \frac{y u_\tau}{\nu}$  and  $u^+ = \frac{u}{u_\tau}$ , where the reference friction velocity is  $u_\tau = \sqrt{\frac{\tau_w}{\rho}}$ , and  $\tau_w$  is the wall shear stress.

### 3.2.1 Deardorff Model

The Deardorff model (1970) [18] is considered to be the first near-wall treatment attempt for LES, although it does not directly model the wall shear stress. Deardorff assumed the turbulence to be isotropic near the wall and enforced the velocities to satisfy the logarithmic velocity profile by defining the second derivatives at the first off-wall grid points. The boundary conditions in the Deardorff model can be expressed as

$$\frac{\partial^2 \bar{u}}{\partial y^2} = -\frac{1}{\kappa y_0^2} + \frac{\partial^2 \bar{u}}{\partial z^2} , \quad (48)$$

$$\bar{v}_w = 0 , \quad (49)$$

$$\frac{\partial^2 \bar{w}}{\partial y^2} = \frac{\partial^2 \bar{w}}{\partial x^2} , \quad (50)$$

where  $y_0$  is the  $y$  coordinate at the first off-wall grid point, and  $z$  is the spanwise direction. In the Deardorff model, wall shear stresses are defined entirely by the subgrid-scale model. This model is very limited since it does not take molecular viscosity into account and ,therefore, is true only in the limit of infinitely high Reynolds numbers.

### 3.2.2 Schumann and Grötzbach Models

The wall-model by Schumann (1975) [19] can be considered as the first true wall-stress model since it directly relates the wall shear stress to the velocity at the first off-wall grid point. The boundary conditions used by Schumann can be expressed as

$$\tau_{xy,w}(x, z) = \frac{\langle \tau_w \rangle}{\langle \bar{u}(x, y_0, z) \rangle} \bar{u}(x, y_0, z) , \quad (51)$$

$$\bar{v}_w = 0 \quad (52)$$

$$\tau_{zy,w}(x, z) = \nu_{SGS} \frac{\bar{w}(x, y_0, z)}{y_0} , \quad (53)$$

where angle brackets denote averaging over a plane parallel to the wall. One major disadvantage in this model is that the mean wall shear  $\langle \tau_w \rangle$  must be known *a priori*, which reduces the value of the model as a predictive method. The mean near wall velocity  $\langle \bar{u}(x, y_0, z) \rangle$  is calculated from the logarithmic law, and the mean wall shear stress can be assigned to be equal to the driving pressure gradient in channel flows. Essentially, the Schumann model only scales the mean wall shear stress with the ratio of the local velocity and the mean velocity to obtain the local wall shear stress in the  $x$ -direction. This kind of velocity scaling is common to all approximative boundary condition approaches. The spanwise wall shear stress in the Schumann model is calculated by assuming the SGS viscosity to be constant within the first LES cell [25].

Later, Grötzbach [20] modified the Schumann model to remove the requirement of the *a priori* known mean wall shear stress. In the Grötzbach model, the mean near wall velocity is calculated by averaging the simulated velocity with respect to time and a homogeneous direction. This formulation enables the mean wall shear stress to be directly calculated from the log-law

$$u^+ = \frac{\langle \bar{u} \rangle}{u_\tau} = \frac{1}{\kappa} \ln y^+ + B , \quad (54)$$

and the expression of the friction velocity

$$u_\tau = \sqrt{\frac{\tau_w}{\rho}} . \quad (55)$$

### 3.2.3 Shifted and Ejection Models

Piomelli et al. [34] proposed further modifications to the Schumann's model in 1989 based on the experimental results of Rajagopalan and Antonia [35]. According to their results, the correlation between the wall shear stress and the velocity improves, if a streamwise displacement  $\Delta_s$  is introduced between the linked velocity node and the wall shear stress. The motivation behind this displacement is the inclined nature of the elongated turbulent structures in the boundary layer, and therefore the input velocity for the wall-model should be taken slightly downstream. The boundary conditions of the shifted model can be expressed as

$$\tau_{xy,w} = \frac{\langle \tau_w \rangle}{\langle \bar{u}(x, y_0, z) \rangle} \bar{u}(x + \Delta_s, y_0, z) , \quad (56)$$

$$\bar{v}_w = 0 , \quad (57)$$

$$\tau_{zy,w} = \frac{\langle \tau_w \rangle}{\langle \bar{u}(x, y_0, z) \rangle} \bar{w}(x + \Delta_s, y_0, z) . \quad (58)$$

The optimal displacement value has been found from the DNS and experimental data, and it is approximately

$$\Delta_s = \begin{cases} Y \cot 8^\circ, & \text{if } 30 < y_0^+ < 50 \\ Y \cot 13^\circ, & \text{if } 50 \leq y_0^+ \end{cases} . \quad (59)$$

This particular model has been found to correlate with the experimental and DNS results better than the standard non-shifted Grötzbach model for plane channel flows.

Another wall-model proposed by Piomelli et al. [34] is the so-called ejection model, which takes into account sweep and ejection phenomena in the boundary layer. The sweep and ejection are rapid motions towards and away from the wall, and they have a considerable effect on the wall shear stress. The ejection decreases the wall shear stress, while sweep increases it. The ejection model is given by boundary conditions

$$\tau_{xy,w} = \langle \tau_w \rangle - C u_\tau \bar{v}(x + \Delta_s, y_0, z) , \quad (60)$$

$$\bar{v}_w = 0 , \quad (61)$$

$$\tau_{zy,w} = \frac{\langle \tau_w \rangle}{\langle \bar{u}(x, y_0, z) \rangle} \bar{w}(x + \Delta_s, y_0, z) , \quad (62)$$

where  $C$  is a dimensionless constant, and the mean wall shear stress is calculated from the log-law. Similarly to the shifted model, the ejection model has been tested only for plane channel flows, and there were no major differences in the results when compared to the shifted model. The applicability of all aforementioned approximative boundary conditions is limited to simple geometries since the plane-averaging  $\langle \rangle$ -operator requires homogeneous flow behavior.

### 3.2.4 Auxiliary Grid Approach: TBLE Model

The auxiliary grid models can be considered as wall-stress models as well, since they calculate the wall shear stress directly from the LES field. However, they differ from the approximative boundary conditions, as they utilize a separate grid to calculate the inner boundary layer. The finer auxiliary grid is typically placed inside the first cell row or rows of the main grid. The coupling between the zones is weak, since the LES quantities only affect the wall shear stress calculation through the boundary condition between the layers. A typical grid structure of auxiliary grid approaches is sketched in Figure 4.

The first auxiliary grid model was proposed by Balaras and Benocci [36] in 1994, and it is usually referred to as the thin boundary layer equation (TBLE) model. As the name suggests, the equations solved within the inner layer are the thin boundary layer equations, which lean on the RANS-type thin shear layer approximation. The simplification is based on the fact that the gradients in the wall-normal direction

are dominant over the gradients in other directions, which allows neglecting the streamwise and spanwise viscous terms [37]. Moreover, the pressure term normal to the wall is also assumed to be negligible. The thin boundary layer equations can be expressed as

$$\frac{\partial \bar{u}_i}{\partial t} + \frac{\partial}{\partial x_i}(\bar{u}_n \bar{u}_i) = -\frac{\partial \bar{p}}{\partial x_i} + \frac{\partial}{\partial x_n} \left[ (\nu + \nu_t) \frac{\partial \bar{u}_i}{\partial x_n} \right], \quad (63)$$

where  $n$  denotes the wall-normal direction within the wall-model and  $i = 1, 2$  or  $i = 1, 3$  depending on the plane orientation. The normal velocity  $u_n$  in Equation (63) can be calculated from the mass balance in the auxiliary grid. The velocity at the first off-wall grid point obtained from the outer flow calculations is used as the free stream boundary condition for the thin boundary layer equations, and no-slip condition is used at the wall. The wall shear stress calculated from the auxiliary TBLE simulation is then applied as the boundary condition to the outer flow calculation to update the first off-wall LES velocities. [38]

Several variations of the thin boundary layer model have been proposed, but they only differ in the eddy viscosity definitions. Balaras et al. [21] used an algebraic eddy viscosity model in their extensive study in which they applied the model to plane channel flows. The expression of the eddy viscosity in Balaras' study is given as

$$\nu_t = (\kappa y)^2 D(y) |\bar{S}|, \quad (64)$$

in which  $D(y)$  is a van Driest-style damping function, which essentially limits the eddy viscosity value in the viscous sublayer. The damping function formulation that Balaras et al. used is defined as

$$D(y) = 1 - \exp[-(y^+/A^+)^3], \quad (65)$$

where  $A^+$  is an adjustable constant, for which they used a value  $A^+ = 25$ .

Naturally, the auxiliary grid approaches are more expensive in terms of computational requirements than the models based on the approximative boundary conditions, since another subsimulation needs to be included. However, they have been found to produce better stress predictions, especially in areas where the equilibrium assumption does not hold. [25]

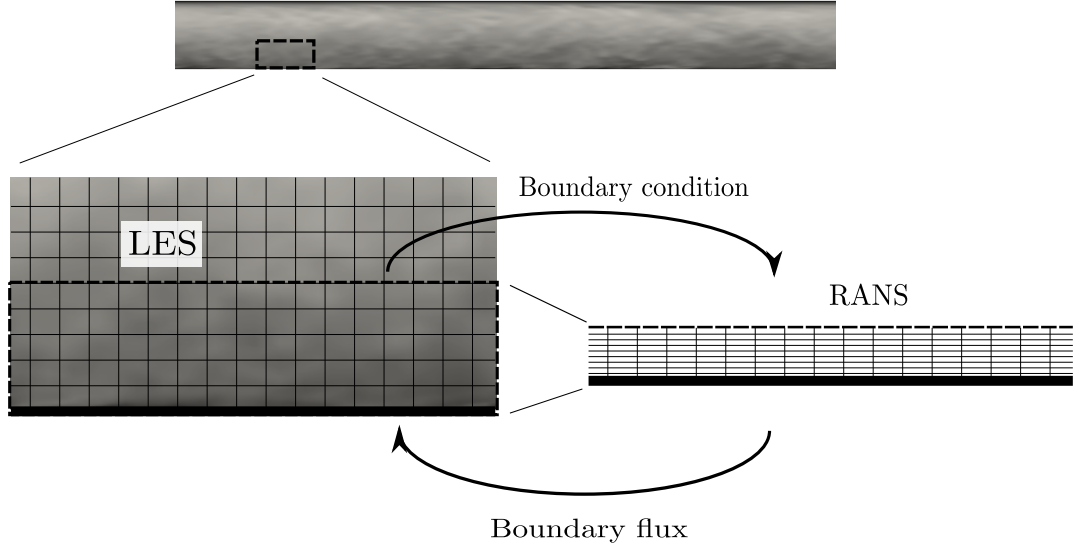


Figure 4: Auxiliary grid model principle.

### 3.2.5 Dynamic Auxiliary Grid Approaches

For complex flows, the regular auxiliary grid approaches can be improved by introducing a dynamic procedure for the eddy viscosity calculation. The principle idea of the dynamic wall-modeling is to take the small amount of resolved Reynolds stresses that are retained in the wall-model layer into account, since the input values are taken from the instantaneous field. Wang & Moin (2002) [22] proposed an approach where the total turbulent stress (resolved+modeled) is matched at the exchange location by dynamically setting the wall-model eddy viscosity to be equal as the SGS eddy viscosity calculated from the LES. This leads to a dynamical adjustment of the von Kármán constant  $\kappa$  in the mixing length model, which can be expressed as

$$\kappa = \frac{\langle \nu_{SGS} \rangle}{\langle y_w^+ (1 - e^{-y_w^+/A^+})^2 \rangle} , \quad (66)$$

where the angular brackets denote averaging in the homogeneous direction as well as over 150 previous time steps. Wang & Moin applied this methodology for a flow over an airfoil and found the results to improve for low to moderate Reynolds numbers.

Kawai & Larsson (2012) [39] applied the aforementioned methodology for a flat-plate boundary layer and found that the eddy viscosity was significantly underestimated at high Reynolds numbers. The authors extended the approach into the compressible framework and proposed an improvement, in which the coefficient  $\kappa$  is a function of  $y^+$ . They motivated this change with the argument that the ratio of the resolved and modeled stress increases with increasing  $y$  and is also dependent on the generally anisotropic wall-normal resolution. In this new methodology, the values of  $\kappa = 0.41$  and  $Pr_t = 0.9$  are kept constant up to a certain critical height  $y_{crit}$ , from which the values are linearly increased to match the stresses at the exchange location. The critical height location  $y$  is suggested to be  $y_{crit} = \alpha' \Delta$ , where

$\Delta$  is the maximum wall-parallel cell dimension, and  $\alpha'$  is a free parameter that needs to be adjusted accordingly to the grid resolution and numerical schemes. The authors used an optimized value of  $\alpha' = 0.48$ .

The most recent dynamic wall-model approach was proposed by Park & Moin (2014) [40]. While the previous dynamic approaches relied on the explicit matching of the turbulent stresses at the exchange location, the new approach adjusts several model constants to account the current turbulence state. The authors start from the requirement that the governing turbulence model needs to model the total Reynolds stresses,

$$2\mu_{t,wm}\bar{S}_{ij}^d - \frac{2}{3}\bar{\rho}k\delta_{ij} - \bar{\rho}\bar{R}_{ij} = 2\mu_t^*\bar{S}_{ij}^d - \frac{2}{3}\bar{\rho}k^*\delta_{ij} , \quad (67)$$

where  $R_{ij} = \overline{u'_i u'_j}$  is the resolved Reynolds stress tensor,  $S^d$  is a notation for the deviatoric part of the strain-rate tensor  $S^d = S_{ij} - \delta_{ij}S_{kk}/3$  and  $k$  is the modeled turbulent kinetic energy. In addition, the superscript  $*$  denotes mixing length modeled quantities and the overbar denotes averaging with respect to time and/or homogeneous direction. In Equation (67), the entire left-hand side represents the total Reynolds stresses and the right-hand side represents the mixing length modeled Reynolds stresses with constant  $\kappa$  and  $Pr$ . The authors reformulate Equation (67) in a least square sense and minimize its  $L_2$  error norm to obtain the expression for the dynamic von Kármán constant to be

$$\kappa_{wm}^2 = \kappa^2 + \frac{\bar{R}_{ij}\bar{S}_{ij}^d}{2\bar{S}_{ij}^d\bar{S}_{ij}^d y^2 |S|D(y)} . \quad (68)$$

Furthermore, the authors extended the wall-model to predict transition by adopting the dynamic turbulence sensor methodology by Bodart & Larsson [41]. The wall-model was tested for a fully turbulent and transitional flat plate boundary layers, and the results were found to be in good agreement with the wall-resolved and experimental data.

### 3.3 RANS/LES Hybrids

Another approach for the near-wall treatment are the RANS/LES hybrids. These models also divide the computational domain into LES and RANS zones, but they differ from the auxiliary grid models by utilizing only a single grid. Therefore, the LES and RANS zone division needs to be defined by a local change in turbulence modeling. A schematic picture of this zone division is illustrated in Figure 5. The most widespread RANS/LES hybrid is the Detached Eddy Simulation (DES) with a modified Spalart-Allmaras turbulence model which was introduced by Spalart et al. [23] in 1997. In DES, RANS equations are solved for attached boundary layers, while LES equations are solved in the core flow and detached regions. In fact, the Unsteady Reynolds Averaged Navier-Stokes (URANS) is a better term to describe the boundary layer calculation, since the strong coupling between the zones causes the inner zone to contain a time scale. [38]

In the modified Spalart-Allmaras model, the transition from LES to RANS is defined by a single variable  $\tilde{d}$ , which is expressed as

$$\tilde{d} = \min(y_w, C_{DES}\Delta) , \quad (69)$$

where  $y_w$  is the distance to the nearest wall,  $C_{DES}$  is a calibrated constant, and  $\Delta$  is the largest cell dimension. In the boundary layer, where the cells are considerably finer in the wall normal direction,  $\tilde{d}$  criterion deploys the turbulence model to behave as traditional RANS type model, since  $y_w < C_{DES}\Delta \rightarrow \tilde{d} = y_w$ . However, in the core flow and separated regions, where the distance to the wall is larger than the cell dimensions  $C_{DES}\Delta < y_w \rightarrow \tilde{d} = C_{DES}\Delta$ , the turbulence model changes to a Smagorinsky type SGS model and the large scales of turbulence are resolved.

One major drawback in DES is the appearance of an artificial buffer layer that results from the time scale collision of the two zones. Since the time scales in the boundary layer calculated by URANS are generally larger than the ones resolved in LES, they tend to become dominating and cause unrealistic behavior near the interface [42]. The so-called buffer layer can extend up to 20 % of the boundary layer height above the RANS/LES interface and typically causes 10-15 % underprediction for the wall shear stress. This unfavorable feature has been partly removed in newer DES variations, such as Delayed Detached Eddy Simulation (DDES) [43] and Improved Delayed Detached Eddy Simulation (IDDES) [44]. These more advanced RANS/LES hybrids are based on artificially delaying the RANS to LES transition in attached boundary layers to prevent grid induced separation and modeled stress depletion when using finer meshes. [45]

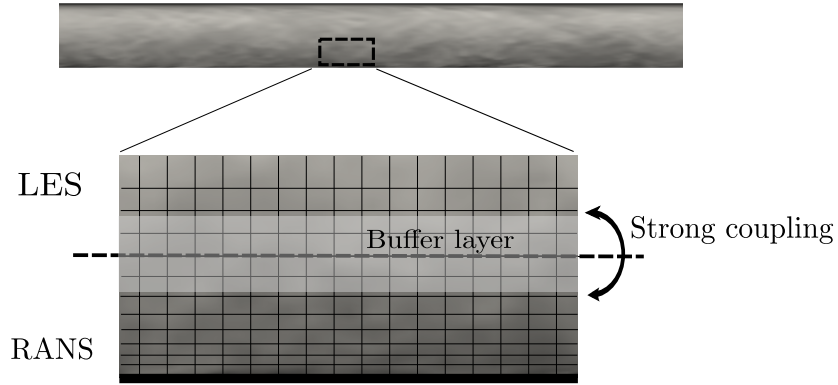


Figure 5: RANS/LES hybrid principle.

## 4 System Rotation

As mentioned earlier, a spanwise rotating channel is the simplest case to study the effects of system rotation. In this chapter, the accelerations resulting from the coordinate transformation will be briefly derived and their effects on the flow quantities in this particular configuration will be discussed. The examination is performed in Reynolds averaged and incompressible sense. Furthermore, the physical flow phenomena that have been identified in several experiments and numerical studies will be presented.

### 4.1 Coriolis and Centrifugal Accelerations

Let us begin by considering an inertial frame with a basis  $(\vec{I}, \vec{J}, \vec{K})$  and a rotating frame with a basis  $(\vec{i}, \vec{j}, \vec{k})$ , which are illustrated in Figure 6. In the figure  $\vec{R}_0$  is the position vector of the rotating coordinate system,  $\vec{R}$  is a position vector of a moving object in inertial coordinate system and  $\vec{r}$  is the position vector of the same moving object in the rotating coordinate system. The position vector of the moving object can be expressed in either coordinate system as

$$\vec{R} = X\vec{I} + Y\vec{J} + Z\vec{K} , \quad \vec{r} = x\vec{i} + y\vec{j} + z\vec{k} . \quad (70)$$

Furthermore, it can also be expressed as the sum of the rotating frame origin vector and position vector in the rotating frame vector

$$\vec{R} = \vec{R}_0 + \vec{r} . \quad (71)$$

By differentiating the expression with respect to time, the relation for the velocity is found to be

$$\frac{d\vec{R}}{dt} = \frac{d\vec{R}_0}{dt} + \frac{dx}{dt}\vec{i} + x\frac{d\vec{i}}{dt} + \frac{dy}{dt}\vec{j} + y\frac{d\vec{j}}{dt} + \frac{dz}{dt}\vec{k} + z\frac{d\vec{k}}{dt} . \quad (72)$$

The expression can be simplified by adopting the definition of angular velocity  $\vec{\omega} = \vec{\Omega} \times \vec{r}$ , which can be written for the individual terms as

$$\frac{d\vec{i}}{dt} = \vec{\Omega} \times \vec{i} , \quad \frac{d\vec{j}}{dt} = \vec{\Omega} \times \vec{j} , \quad \frac{d\vec{k}}{dt} = \vec{\Omega} \times \vec{k} , \quad \frac{d\vec{R}_0}{dt} = \vec{\Omega} \times \vec{R}_0 . \quad (73)$$

By substituting the expressions above into Equation (72), the following form for the velocity is obtained

$$\frac{d\vec{R}}{dt} = \vec{\omega} + \vec{\Omega} \times \vec{R}_0 + \vec{\Omega} \times \vec{r} = \vec{\omega} + \vec{\Omega} \times \vec{R} . \quad (74)$$

The relation for the acceleration can be found by differentiating Equation (74) with respect to time

$$\begin{aligned}
\frac{d^2 \vec{R}}{dt^2} &= \frac{d}{dt}(\vec{v} + \vec{\Omega} \times \vec{R}) \\
&= \frac{d^2 x}{dt^2} \vec{i} + \frac{dx}{dt} \frac{d\vec{i}}{dt} + \frac{d^2 y}{dt^2} \vec{j} + \frac{dy}{dt} \frac{d\vec{j}}{dt} + \frac{d^2 z}{dt^2} \vec{k} + \frac{dz}{dt} \frac{d\vec{k}}{dt} + \vec{\Omega} \times \frac{d\vec{R}}{dt} \\
&= \vec{a} + \vec{\Omega} \times \vec{v} + \vec{\Omega} \times (\vec{v} + \vec{\Omega} \times \vec{R}) \\
&= \vec{a} + 2\vec{\Omega} \times \vec{v} + \vec{\Omega} \times (\vec{\Omega} \times \vec{R}) .
\end{aligned} \tag{75}$$

In the expression above, the term  $2\vec{\Omega} \times \vec{v}$  is the Coriolis acceleration and  $\vec{\Omega} \times (\vec{\Omega} \times \vec{R})$  is the centrifugal acceleration. These acceleration are fictitious and do not represent any real forces. They are generated as compensatory terms for the real accelerations to take into account the fact that the observer is rotating. [46]

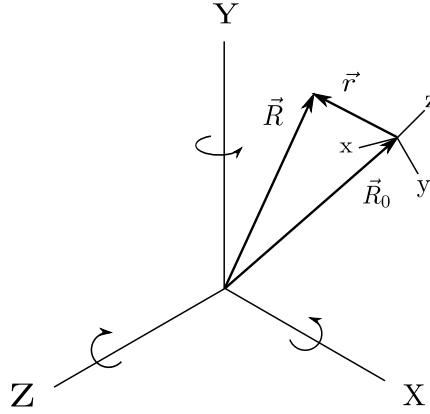


Figure 6: Inertial and rotating coordinate systems.

## 4.2 Spanwise Rotating channel: Average Quantities

Since the Navier-Stokes momentum equation essentially represents the Newton's second law, transforming it to the rotating frame introduces the previously derived fictitious accelerations to its right-hand side. The incompressible Navier-Stokes equations in a rotating reference frame are given by

$$\frac{\partial u_i}{\partial x_i} = 0 , \tag{76}$$

$$\frac{\partial u_i}{\partial t} + u_j \frac{\partial u_i}{\partial x_j} = -\frac{1}{\rho} \frac{\partial p_{eff}}{\partial x_i} + \nu \frac{\partial^2 u_i}{\partial x_j \partial x_j} + 2\epsilon_{ij3} u_j \Omega_k , \tag{77}$$

where the final term in the momentum Equation (77) is the Coriolis force, and  $\epsilon_{ij3}$  is the Levi-Civita tensor, which corresponds to the cross product. The Levi-Civita

tensor is defined as

$$\varepsilon_{ijk} = \begin{cases} +1 & \text{when } (i, j, k) = (1, 2, 3), (2, 3, 1) \text{ or } (3, 1, 2), \\ -1 & \text{when } (i, j, k) = (3, 2, 1), (1, 3, 2) \text{ or } (2, 1, 3), \\ 0 & \text{when } i = j \text{ or } j = k \text{ or } k = i . \end{cases} \quad (78)$$

The tensor index  $k$  is fixed to a value of three, since only a spanwise rotation is considered. When the flow is acknowledged to be incompressible, the centrifugal force can be expressed as a force potential, which can be integrated into the effective pressure as

$$p_{eff} = p - \frac{1}{2}\rho\Omega^2 r^2 . \quad (79)$$

For the algebraic analysis, it is convenient to do the Reynolds decomposition by dividing flow quantities into the mean and the fluctuating part as  $u = \bar{U} + u'$ . By assuming a steady-state situation, the Reynolds averaged momentum equation is obtained

$$\bar{U}_j \frac{\partial \bar{U}_i}{\partial x_j} = -\frac{1}{\rho} \frac{\partial \bar{p}_{eff}}{\partial x_i} + \nu \frac{\partial^2 \bar{U}_i}{\partial x_j \partial x_j} - \frac{\partial \overline{u'_i u'_j}}{\partial x_j} + 2\varepsilon_{ij3} \bar{U}_j \Omega_k , \quad (80)$$

where the term  $\frac{\partial \overline{u'_i u'_j}}{\partial x_j}$  is the Reynolds stress tensor, representing all turbulent activities. In case of a fully developed channel flow, the mean velocity in the  $y$ -direction  $\bar{V}$  is zero, and mean velocity in the  $x$ -direction  $\bar{U}$  is only a function of  $y$ . Moreover, with a relatively rapid rotation rates  $0.1 < Ro < 1$ , lower magnitude Reynolds stresses can be neglected [12], and the momentum equations in  $x$ - and  $y$ -directions can be written individually as

$$0 = -\frac{1}{\rho} \frac{\partial p_{eff}}{\partial x} + \frac{d}{dy} \left( \nu \frac{d\bar{U}}{dy} - \overline{u'v'} \right) , \quad (81)$$

$$2\Omega\bar{U} = -\frac{1}{\rho} \frac{\partial p_{eff}}{\partial y} . \quad (82)$$

Noteworthy in Equations (81) and (82) above is that, the Coriolis acceleration affects the mean flow only through the Reynolds stress component, which imparts that the mean velocity profile of a fully laminar flow would remain unaffected. From the  $y$ -direction momentum equation, it is also noticed that a negative pressure gradient is generated as the balancing force to the Coriolis acceleration. This leads to a pressure difference between the walls, and it can be deduced that the pressure on the upper wall channel is lower than on the lower wall for positive rotation rates. From now on, these different sides will be referred to as the suction (low pressure) and pressure (high pressure) side.

From Equation (82) it is also seen that the flow normal pressure gradient  $\frac{\partial p_{eff}}{\partial y}$  is not proportional to  $x$ . Thus, the term  $\frac{\partial p_{eff}}{\partial x}$  is a constant and Equation (81) can be

integrated from  $y_{wall}$  to an arbitrary point  $y$  to obtain the expression for the total shear

$$\nu \frac{d\bar{U}}{dy} - \overline{u'v'} = \nu \frac{d\bar{U}}{dy} \Big|_{y=y_{wall}} + \frac{1}{\rho} \frac{\partial p_{eff}}{\partial x} (y - y_{wall}) . \quad (83)$$

Various experiments have shown that the wall turbulence is enhanced on the pressure side and dampened on the low-pressure side [12]. Because of these differences in turbulence levels, the magnitude of wall shear stress term  $\tau_w = \nu \frac{d\bar{U}}{dy} \Big|_{y=y_{wall}}$  in Equation (83) depends on whether the integration is started from the stabilized or destabilized wall. However, since the total shear is constant for the entire channel, Equation (83) can be written as

$$\frac{\tau_{wp} + \tau_{ws}}{2h} = \frac{\partial p_{eff}}{\partial y} , \quad (84)$$

where the subscript  $p$  denotes the pressure and  $s$  the suction wall. Furthermore, by introducing the expression of the wall shear velocity

$$u_\tau = \sqrt{\frac{\tau_w}{\rho}} , \quad (85)$$

Equation (84) can be further modified into

$$u_\tau = \sqrt{-\frac{h}{\rho} \frac{\partial p_{eff}}{\partial x}} , \quad (86)$$

where  $u_\tau$  is the global friction velocity defined as

$$u_\tau^2 = \frac{1}{2}(u_{\tau p}^2 + u_{\tau s}^2) . \quad (87)$$

In the literature, this friction velocity is used to scale all results that are presented wall units and this is the convention we follow, unless otherwise mentioned.

### 4.3 Coriolis Stability

As briefly mentioned in the previous section, the Coriolis acceleration affects the local stability of the flow. These effects can be studied with a local non-dimensional parameter called the gradient Richardson or Bradshaw-Richardson number [11]. System rotation has a destabilizing effect on the region where the gradient Richardson number is negative, and on the contrary stabilizing effect where it is positive. The gradient Richardson number for a rotating system is defined as

$$Ri = S(S + 1) , \quad (88)$$

where

$$S = -\frac{2\Omega}{(\partial \bar{U} / \partial y)} . \quad (89)$$

In a spanwise rotating channel flow, the mean velocity profile has been found to follow the  $2\Omega$  slope in the core flow where the Coriolis stability is neutral. A schematic picture of a typical stability region flow is illustrated in Figure 7. From the expression of the gradient Richardson number it can be deduced that near the suction side where the mean velocity gradient is below the value of background vorticity, the flow is locally stabilized. On the contrary, near the high-pressure side, the flow is locally destabilized, since the velocity gradient is dominant over the background vorticity.

Stability changes resulting from the Coriolis acceleration have major effects on the flow characteristics. Several studies have been performed to identify the physical phenomena occurring within these destabilized and stabilized regions. Johnston et al. [12] observed three stability related phenomena based on their experiments on a spanwise rotating channel flow. Firstly, the rate of wall-layer streak bursts increases and decreases on the pressure and suction side, respectively. This is the main reason for the local increase or decrease in the turbulence production, and thereby also the change in the mean velocity profile and the local wall shear stresses. Secondly, the Coriolis acceleration can completely suppress or delay the transition of the laminar boundary layer on the stabilized suction side. Thirdly, counter rotating Taylor-Görtler type of vortices are generated in spanwise direction. The authors also found that these large scale roll cells tend to move towards the pressure side with increasing Rotation number.

In later studies Wallin et al. [17] and Brethower et al. [47] discovered cyclic instabilities in their DNS simulations when the flow is locally close to laminarization. The authors pointed out that high rotation rates suppress the oblique modes of the flow, but the two-dimensional plane modes which resemble the Tollmien-Schlichting (TS) waves, remain unaffected. The cycle where the TS waves grow, become unstable and finally break down into turbulence affects the flow quantities and can be observed as temporal spikes in the Reynolds and wall shear stresses. According to their results, if the rotation rate is moderately high, the growth of the TS waves is confined to the suction side. However, by further increasing the rotation rate close to the critical value where both sides laminarize, similar behavior begins to occur also on the pressure side. [47]

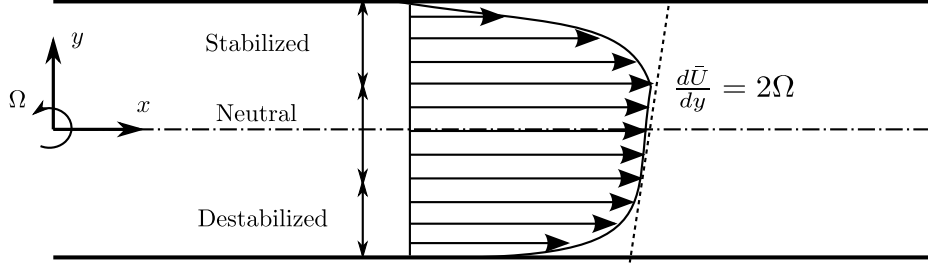


Figure 7: A schematic illustration of a typical mean velocity profile and the stability zone division.

#### 4.4 Reynolds Stresses

To support the interpretation of the simulation results it is convenient to discuss explicitly how the rotation affects each component of Reynolds stresses. The transport equation of Reynolds stresses is defined as

$$\frac{\partial \overline{u'_i u'_j}}{\partial t} + \bar{U}_k \frac{\partial \overline{u'_i u'_j}}{\partial x_k} = \mathcal{P}_{ij} + \Pi_{ij} - \epsilon_{ij} + \mathcal{D}_{ij} + \mathcal{C}_{ij} , \quad (90)$$

where the terms on the right-hand side of the equation represent shear production, pressure-strain, dissipation, diffusion and Coriolis effect, respectively. In this context it is sufficient to only examine the shear production and Coriolis terms, which are defined as

$$\mathcal{P}_{ij} = \overline{u'_i u'_m} \frac{\partial \bar{U}_j}{\partial x_m} - \overline{u'_j u'_m} \frac{\partial \bar{U}_i}{\partial x_m} , \quad (91)$$

$$\mathcal{C}_{ij} = -2\Omega_k (\overline{u'_i u'_m} \epsilon_{mjk} - \epsilon_{imk} \overline{u'_m u'_j}) \quad (92)$$

By writing the tensors in a component form for a fully developed flow  $\bar{U} = \bar{U}(y)$ , the only non-vanishing terms are

$$\mathcal{P}_{11} = -2\overline{u'v'} \frac{d\bar{U}}{dy} , \quad (93)$$

$$\mathcal{P}_{12} = -\overline{v'^2} \frac{d\bar{U}}{dy} , \quad (94)$$

$$\mathcal{C}_{11} = 4\Omega \overline{u'v'} , \quad (95)$$

$$\mathcal{C}_{22} = -4\Omega \overline{u'v'} , \quad (96)$$

$$\mathcal{C}_{12} = -2\Omega (\overline{u'^2} - \overline{v'^2}) . \quad (97)$$

From the equations above, it can be seen that there are no  $\mathcal{P}_{22}$  and  $\mathcal{P}_{33}$  components, and thus no direct production of  $\overline{v'v'}$  or  $\overline{w'w'}$ . They are, however, present resulting from the energy transfer by pressure-strain interactions. In a non-rotating case,  $\overline{u'v'}$  is known to have the opposite sign as  $\frac{d\bar{U}}{dy}$ , which ensures the positiveness of  $\mathcal{P}_{11}$  in the whole domain [1]. Furthermore, since  $\frac{d\bar{U}}{dy}$  has the opposite sign than the  $y$  coordinate,  $\mathcal{P}_{12}$  is found to always have the same sign as  $y$ .

For positive rotation rates, the destabilized side (pressure side) is on the lower wall where  $y < 0$  and stabilized side (suction side) is on the upper wall where  $y > 0$ . Thus, it can be deduced from signs of the Coriolis Reynolds stress components that increasing positive rotation is directly supposed to decrease  $\overline{u'u'}$  and increase  $\overline{v'v'}$  on the destabilized side, and the effect should be the opposite for the stabilized side. In addition, the term  $\mathcal{C}_{12}$  is expected to decrease  $\overline{u'v'}$  in the whole domain, when assuming  $\overline{u'u'} > \overline{v'v'}$ , which normally is the case. However, rotation naturally has several indirect effects due to cross-relations. For example, the rotation induced reduction in  $\overline{v'v'}$  on the stabilized side further reduces the shear production  $\mathcal{P}_{12}$  as well as Coriolis term  $\mathcal{C}_{12}$ . Due to these complex cross-relations, this kind of examination does not give a complete picture of the Reynolds stress behavior, especially for high rotations rates, but give a preliminary insight about the trends to be expected.

## 5 Low Re Simulation: Rotating Frame Validation

### 5.1 Charles<sup>X</sup> solver

The solver utilized in this project is the compressible LES/DNS in-house solver Charles<sup>X</sup> originally developed at the Center for Turbulence Research, Stanford University. More recently, ISAE-SUPAERO joined the development, and therefore it is available at the department.

Charles<sup>X</sup> supports an unstructured grid topology for arbitrary cell shapes, and solves the filtered Navier-Stokes equations for conserved variables: Mass, momentum and total energy. The SGS stresses are modeled using either the Vreman or the dynamic Smagorinsky model. The SGS heat flux is modeled by the gradient hypothesis and strong Reynolds analogy with a fixed Prandtl and Schmidt numbers. [48]

A solution-adaptive approach with second to fourth order schemes are used to as the discretization method for perfectly regular grids. The computational domain is partitioned with ParMETIS library and the parallel computing is performed with MPI. The time-integration is done by a three-stage third-order Runge-Kutta scheme. [48]

### 5.2 Setup

In order to validate the solver and the Coriolis source terms, a low Reynolds number simulation was performed and compared to the reference data by Kristoffersen & Anderson's [1] DNS simulations. The Reynolds number was approximately 2900 as in the reference case, and the Rotation number was chosen to be 0.5. A negative value for the angular velocity was used as in the reference case, which naturally swaps the suction and pressure side compared to the preliminary discussion in Chapter 4. Furthermore, the same computational domain dimensions were used as in the reference case:  $L_x L_y L_z = 4\pi h \times 2h \times 2\pi h$ . The total number of cells used was 3 million and they were divided in different directions as  $n_x n_y n_z = 200 \times 100 \times 150$ . Although the purpose of the study is the wall-modeling aspect, the inner layer was fully resolved in this simulation for the sake of validation, and the mesh was refined near both walls to ensure  $y^+ < 1$ . The *a posteriori* measurement of the grid parameters was found to produce  $\Delta x^+ \approx 8$  and  $\Delta z^+ \approx 6$ , which lead to the subgrid-scale modeled part to be almost negligible [32].

Periodic boundary conditions were set in  $z$  and  $y$  directions due to the homogeneity. When using a periodic domain, the size of the domain needs to be large enough in order to capture all the necessary scales and to avoid correlation between the periodic values. However, since we are reproducing the simulation by Kristoffersen & Anderson, the sufficiency of the domain size was not investigated. A constant flow rate was ensured by using an adaptive momentum source term, and the bulk Mach number was set as  $Ma = 0.2$ . The adaptive momentum source term and periodicity also prevents thermovariation, which would result from the pressure loss at the wall. In addition, the reference temperature of the fluid and

the wall were set as equal. The Vreman model was chosen as the SGS model, and turbulence was excited by superimpositioning random fluctuations into the initial flow field. The Coriolis force was taken into account with additional source terms, which were added into the  $x$ - and  $y$ -direction momentum equations separately. The Coriolis acceleration component for a spanwise rotating flow is  $2\Omega\rho u$  in  $x$ -direction and  $-2\Omega\rho v$  in  $y$ -direction.

The simulation was performed with a local cluster using 128 cores. The simulation was first run into a steady state, where the turbulence was found to be fully developed. Consequently, the statistical sampling was started and the simulation continued until a statistical convergence was reached.

### 5.3 Post-Processing

Charles<sup>X</sup> solver produces solution files in the generic unstructured VTK data format (.vtu). Due to the nature of the unstructured FVM solver, the solution points for the cell data are not explicitly defined. Therefore, the most convenient approach for post-processing is to exchange the cell data to point data at cell corners and to remove duplicates. These steps can be easily done with Paraview's CleanToGrid and CellDataToPointData functions. The methodology of the CellDataToPointData function is to 'extrapolate' the point data value by averaging the values of each surrounding cell.

All post-processing in this thesis was performed within Paraview's Python shell, and visualizing was mainly done with regular Python's Matplotlib library by extracting the wanted data from the VTK point data using Paraview's numpy\_support library. All time-averaged quantities were also spatially averaged in  $x$  and  $z$ , since the flow quantities are homogeneous in these directions. The spatial averaging can be done by slicing the domain for each  $y$ -coordinate, integrating the variables in the  $xz$ -planes and dividing the integrated values by the plane areas. This procedure provides quicker convergence for the flow statistics, since the amount of uncorrelated samples is increased.

### 5.4 Results

The phenomena resulting from the Coriolis effect listed in Chapter 4 were identified in the results. Figure 8 presents the simulation configuration and instantaneous velocity magnitudes. On the lower wall of the channel, the turbulence is clearly dampened, which can be seen as a laminar like boundary layer, while upper side still remains fully turbulent. Figure 9 illustrates the secondary flow velocity lines of the velocity vector  $\vec{V} = v\vec{j} + w\vec{k}$  on the  $zy$ -plane at  $x = L/2$ . These shapes clearly indicate the appearance of large scale roll cells on the unstable side, as Johnston et al. [12] depicted.

The statistical values were found to be in good agreement with the reference data. Figure 10 shows the mean velocity profile in the outer layer scaling as well as in wall units. The mean velocities in wall units were made dimensionless with their respective friction velocities  $u_\tau^s$  and  $u_\tau^p$  depending on the wall. From Figure 10, it can

be seen that in the outer layer scaling, the velocity profile almost perfectly matches the DNS results, and the flow in the core region clearly follows the  $2\Omega$  slope, which is also plotted in the figure. However, in wall units, minor differences in the results can be observed, which are resulting from the differences in the resolved wall shear stresses. The friction Reynolds number  $Re_\tau = \rho u_\tau h / \mu$  was found to be overestimated by 1.5 % and 4.5% for the suction and pressure side, respectively. The Reynolds stresses are presented in Figure 11. They are generally in good agreement with the reference data, despite the small overprediction of  $\overline{u'u'}^+$  near the pressure wall. No further analysis, such as grid convergence study, was performed as the current results already give confidence on the validity of the source term implementation.

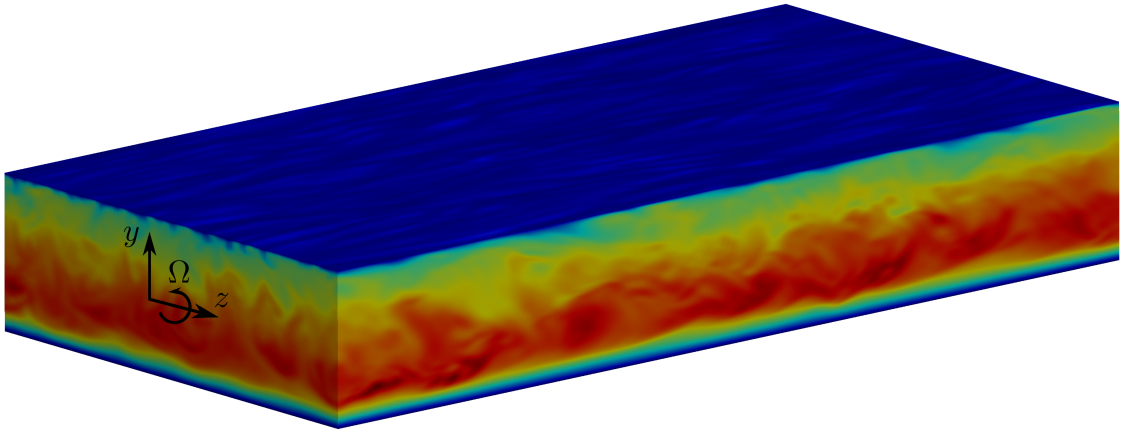


Figure 8: Simulation configuration visualized with instantaneous velocity field when  $Re = 2900$  and  $Ro = 0.5$ .

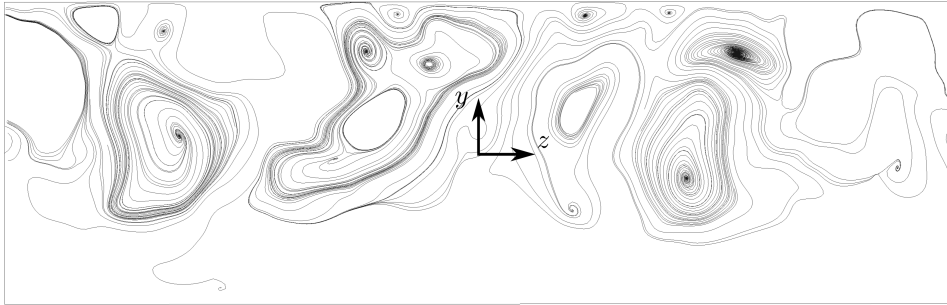


Figure 9: Secondary flow velocity lines in an  $yz$ -plane, depicting the spanwise roll cells.

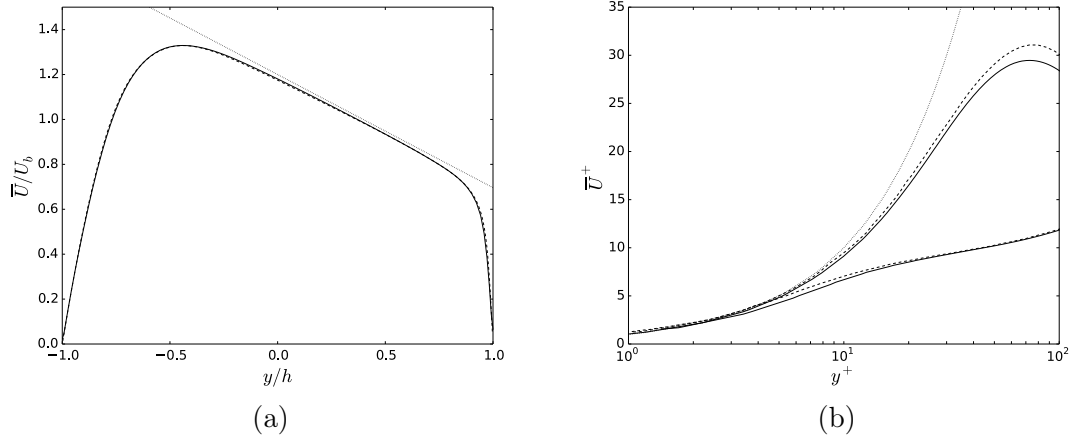


Figure 10: LES —, Kristoffersen & Andersson DNS ---,  $2\Omega$ -slope/Laminar velocity profile ..... (a) Mean velocity profile in the outer layer scaling when  $Re = 2900$  and  $Ro = 0.5$ . (b) Mean velocity profiles in respective wall units.

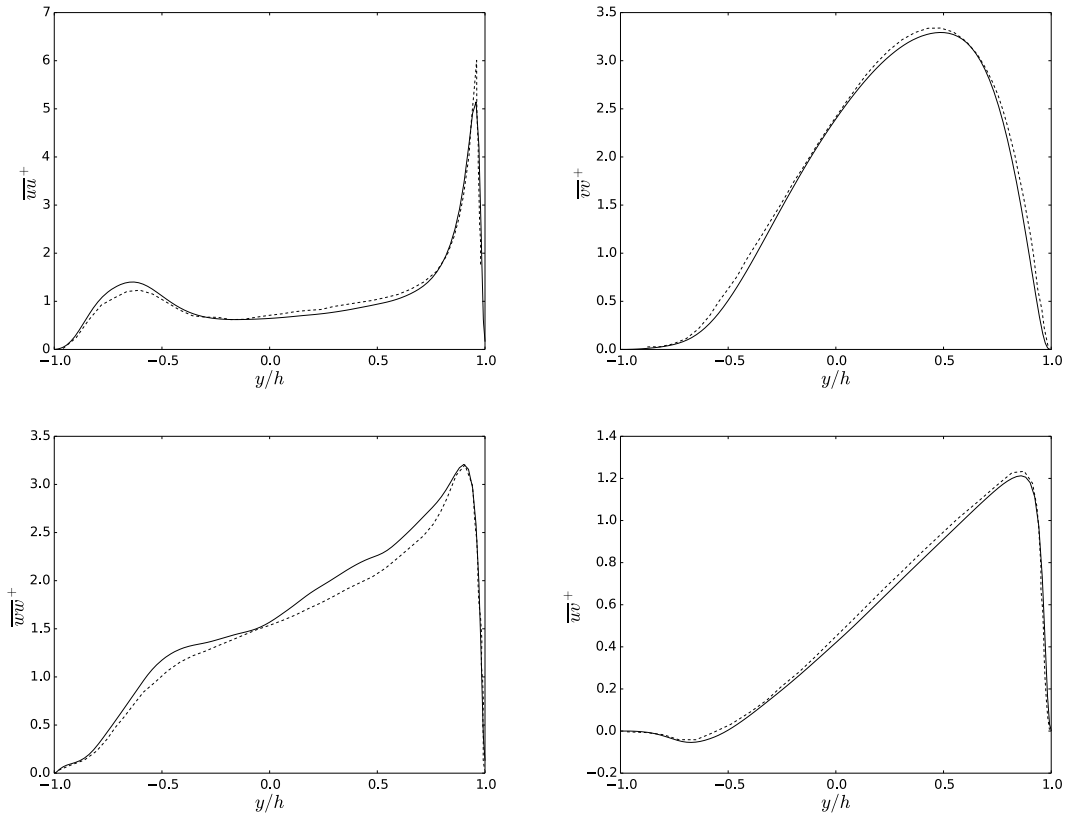


Figure 11: LES —, Kristoffersen & Andersson DNS ---. Reynolds stresses when  $Re = 2900$  and  $Ro = 0.5$ .

## 6 High Re Simulation: Reference Data for Wall-Model investigation

### 6.1 Setup

Very few reference cases of high Reynolds number simulations of a spanwise rotating channel can be found in the literature. Thus, wall-resolved high Reynolds number simulations were performed to obtain data for the wall-model analysis, and the DNS simulation of Brethower et al. [47] was chosen as the general guideline for the current simulations.

The simulations were performed with a bulk Reynolds number around 20 000 as in the DNS of Brethower et al. Three different Rotation numbers were studied: A relatively low  $Ro = 0.15$ , a moderate  $Ro = 0.45$  and a relatively high  $Ro = 1.2$ . The computational domain was chosen to be  $L_x L_y L_z = 8\pi h \times 2h \times 3\pi h$ , and the number of cells in every simulation was 10.5 million,  $n_x n_y n_z = 350 \times 100 \times 300$ . The initialization was done in a 3 million cell mesh, from which the intermediate result was interpolated into the finer mesh. Otherwise, the same simulation parameters and boundary conditions were used as in the validation case. Table 1 gathers the grid resolution details for each simulation. The  $\Delta y^+$  values in the table represent the first off-wall cell heights and a stretching coefficient of 1.05 was used in the refined inner layer region. In the *a posteriori* grid examination, the  $z$ -resolution was found to be slightly above the guideline values suggested by Choi & Moin [32] on the pressure side for the two lower Rotation number cases. However, this small overstep in the resolution is not expected to cause major error in the wall shear stress magnitude, which is the primary attribute for the modeling, and even coarser spanwise resolutions can be found in literature [39]. The maximum average eddy viscosity ratio  $\mu_t/\mu$  was found to be 2.0, which occurs at the pressure side  $y_p^+ \approx 540$ .

$Re$	$Ro$	$\Delta x_p^+$	$\Delta y_p^+$	$\Delta z_p^+$	$\Delta x_s^+$	$\Delta y_s^+$	$\Delta z_s^+$
20 000	0.15	80	0.92	35	54	0.62	23
20 000	0.45	78	0.90	34	36	0.42	16
20 000	1.2	45	0.51	19	24	0.27	10

Table 1: Summary of the simulation cases and grid parameters. Subscripts  $p$  and  $s$  denote the pressure and suction side, respectively.

### 6.2 Results

#### 6.2.1 Mean Statistics

The mean statistics of the three wall-resolved simulations are briefly studied to investigate the  $Ro$  dependency, since it is a crucial aspect for understanding how the wall-model needs to adapt to the system rotation. Average velocity profiles of all three cases in the outer layer scaling and in wall units are presented in Figure

12. Overall, the results show a similar trend as in the reference case, and it can be seen that all mean velocity profiles follow the  $2\Omega$  slope in the core flow. In wall units, the increase in the rotation number tends to move the suction side profiles towards a laminar (parabolic) profile and thicken the viscous sublayer. On the pressure side, the effect is opposite and the curves shift downwards diverging from the standard viscous sublayer earlier. The distinctive behavior of the pressure side curve of  $Ro = 1.2$  can be explained with the fact that the neutral  $2\Omega$  slope region lengthens with increasing  $Ro$ . This leads to a smaller destabilized zone which combined with the adverse pressure tends to significantly shorten the logarithmic layer. If the rotation rate would be further increased, the length of the destabilized region would continue decreasing and finally the velocity profiles would start approaching the laminar profile on the pressure side as well.

Figure 13 shows the Reynolds stresses normalized with global friction velocities. In the graphs, it is visible that near the pressure wall, that  $\overline{u'u'}^+$  decrease and  $\overline{v'v'}^+$  increase with increasing rotation number. On the suction side the behavior is opposite. However, these curves are not directly comparable with the preliminary investigation of the Reynolds stress transport equation, since they are in wall units and the wall shear stresses vary between the cases. The dimensional Reynolds stresses were found to behave similarly and as predicted for  $\overline{u'u'}$  on the pressure side and for  $\overline{v'v'}$  on suction side. The main difference observed was that the  $\overline{u'u'}$  is also dampened on the suction side unlike the preliminary study predicted. This suggests that the direct shear production is significantly dominant over the Coriolis production, which causes the reduction in total production due to the lowered wall shear stress. Furthermore, the drop in  $\overline{u'u'}$  on the destabilized side for  $Ro = 1.2$  was found to be so large, that it causes  $\mathcal{C}_{12} = -2\Omega(\overline{u'^2} - \overline{v'^2})$  to locally change sign. This leads to a local decrease in the negative level of  $\overline{u'v'}$  that explains the peculiar behavior of the  $\overline{u'v'}^+$  curve with  $Ro = 1.2$ . In this particular case, almost a fully laminar region on the stabilized side can be identified, which is associated with the very low values of all Reynolds stresses.

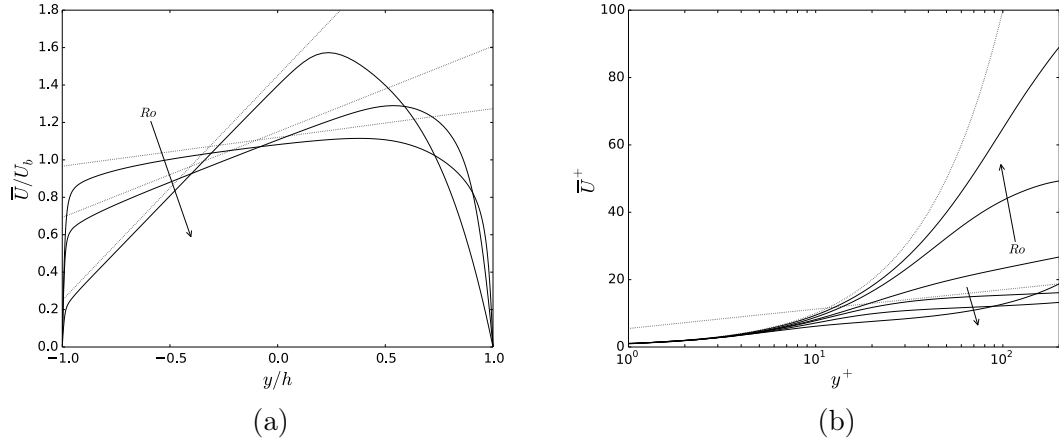


Figure 12: LES —,  $2\Omega$ -slope/log-law/laminar profile ..... . Arrows depict increasing  $Ro$ . (a) Mean velocity profiles in the outer layer scaling when  $Re \approx 20\,000$  and  $Ro = 0.15, 0.45, 1.2$ . (b) Velocity profiles in respective wall units.

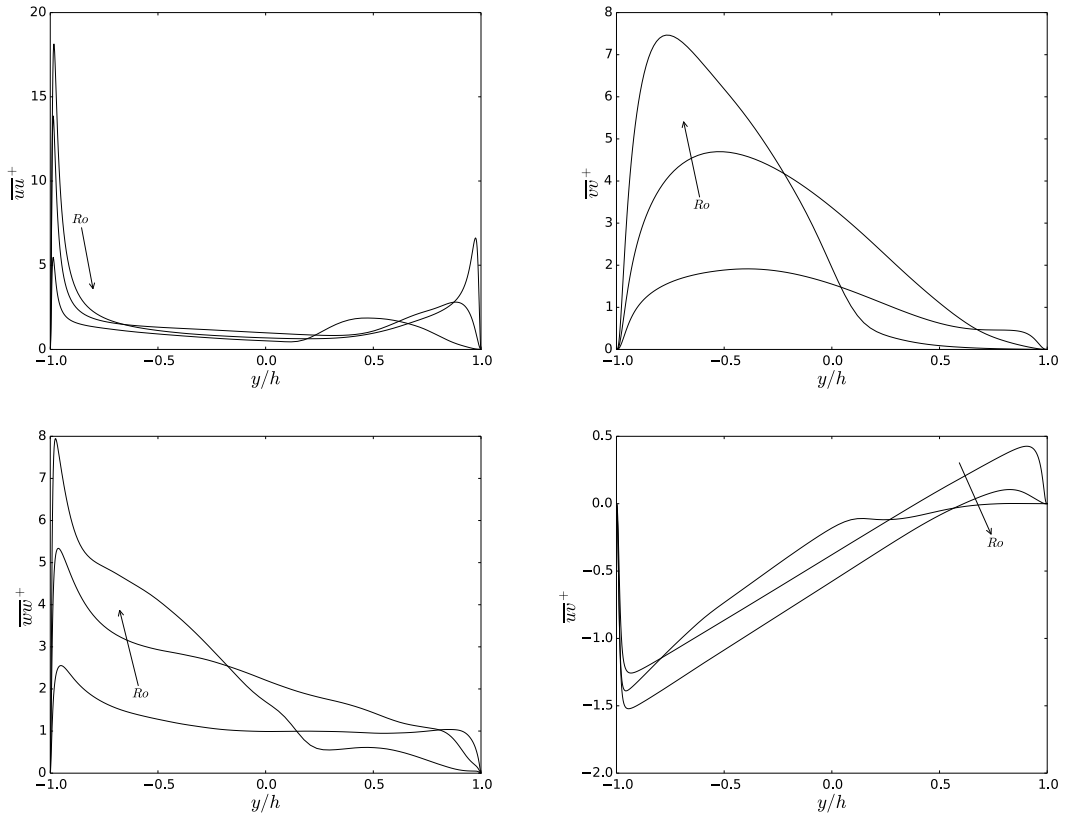
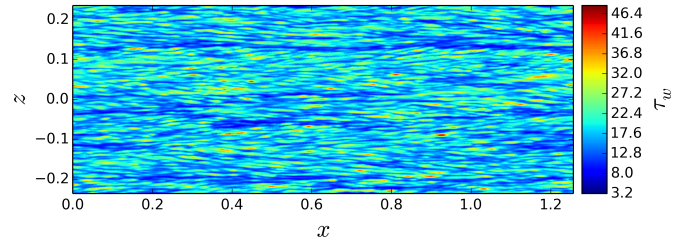


Figure 13: Arrows depict increasing  $Ro$ . Dimensionless Reynolds stresses when  $Re \approx 20\,000$  and  $Ro = 0.15, 0.45, 1.2$ .

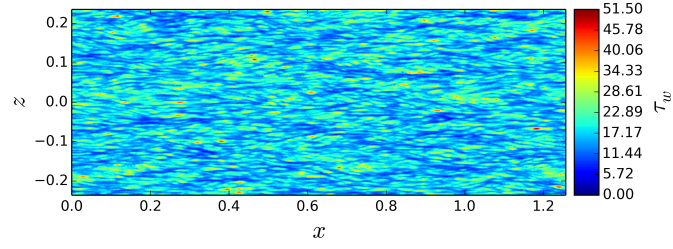
### 6.2.2 Wall Shear Stress Patterns

An interesting aspect regarding wall-modeling is also the behavior of instantaneous wall shear stresses and their local structures. In every case, the pressure side was found to be fully turbulent regardless of the significant drop in wall shear stress magnitudes with  $Ro = 1.2$  as observed in Figure 14. However, small differences can be identified in the wall turbulence structures as the streaks seem to shorten with increasing rotation rate. In terms of wall-modeling, these patterns do not seem alarming, as the flow seems to be in an equilibrium state in all cases.

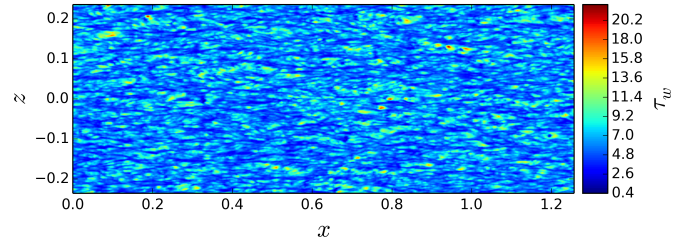
More complex phenomena can be observed on the suction side, which seem to be in a weakly turbulent transitional state for the two lower rotation rates. With the lowest rotation rate  $Ro = 0.15$ , the turbulent areas on the suction side are constantly present and form long ribbon shaped structures that can be seen in the suction side wall shear stress pattern visualizations in Figure 15. With  $Ro = 0.45$ , the turbulent areas were found to become more arbitrary shaped, and they tend to grow and shrink in a long time scale. This behavior can be also identified as periodic deviation in the time dependent and spatially averaged wall shear stress graph in Figure 16. Similar periods was also noticed in the  $Ro = 0.15$ , but they were not as distinctive since the turbulence ribbons were constantly present. This behavior is most likely resulting from the of periodic boundary conditions as the elongated structures tend to become so large that they correlate over the domain in the streamwise direction. Regarding the wall-modeling, these local turbulent spots and the periodic behavior might become problematic to capture, since the phenomena seems to be confined very close to the wall. With  $Ro = 1.2$ , the variation in wall shear stress magnitudes is very low compared to the other cases and the pattern has evolved into more laminar like. The initial forms of plane waves can also be observed as Wallin et al. depicted [17].



(a)



(b)



(c)

Figure 14: Instantaneous wall shear stress field on the pressure side when  $Re \approx 20\,000$ . (a)  $Ro = 0.15$ . (b)  $Ro = 0.45$  (c)  $Ro = 1.2$ . N.B. The differences in the color bar scales.

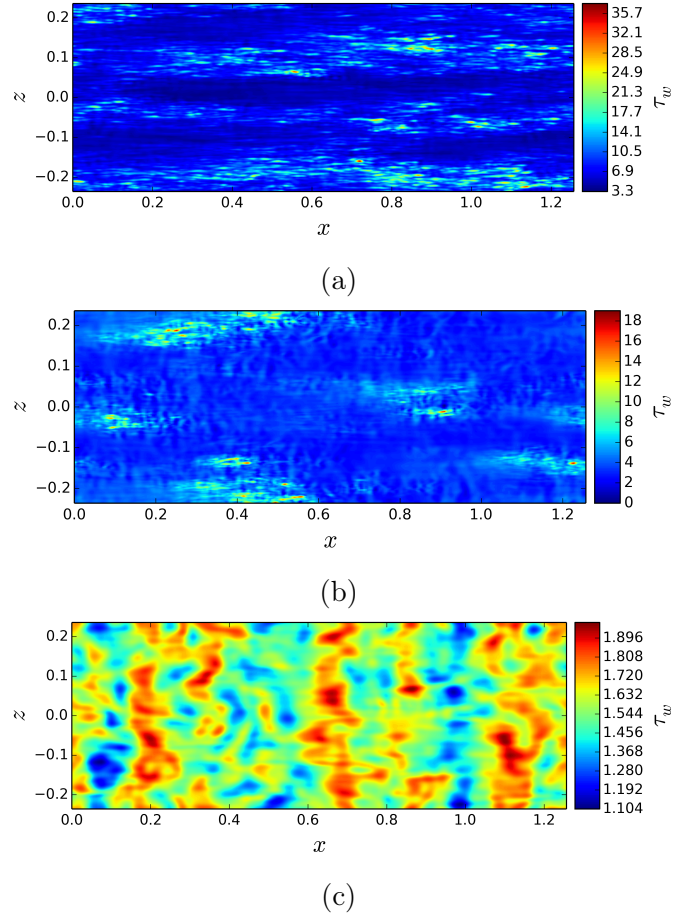


Figure 15: Instantaneous wall shear stress field on the suction side when  $Re \approx 20\,000$ . (a)  $Ro = 0.15$ . (b)  $Ro = 0.45$  (c)  $Ro = 1.2$ . N.B. The differences in the color bar scales.

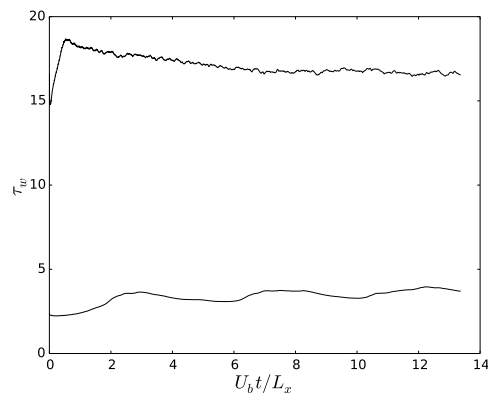


Figure 16: Time dependent, spatially averaged wall shear stress over time when  $Re \approx 20\,000$  and  $Ro = 0.45$ . Periodic behavior on the suction side (lower curve).

### 6.2.3 Spectral Analysis

Two-point correlations were investigated to provide information about the sufficiency of the domain size and to investigate the length scales of turbulent structures. Only the simulation with  $Ro = 0.45$  was studied, as it represents the most complex situation in terms of turbulent behavior.

The two-point correlation function tells us how the velocity fluctuations correlate with each other, and allows us to extract characteristic length scales of energy carrying turbulence structures. The two-point correlation normalized by the one-point correlation and expressed in terms of an autocorrelation coefficient is mathematically defined as

$$R_{ii}(x, r) = \frac{\overline{u'_i(x+r)u'_i(x)}}{\overline{u'^2_i}} , \quad (98)$$

where  $r$  is the distance from the initial point. The correlations were calculated in the streamwise and spanwise directions for each velocity component at each  $y$ -location. This procedure essentially leads to a convolution operation. In order to produce a quicker convolution algorithm, it is convenient to Fourier transform (Python's `numpy.rfft`) the velocity fields into Fourier space, since the Convolution theorem states

$$R_{ii}^*(x, r) = \int_0^{L_x} u'_i(x+r)u'_i(x)dx , \quad (99)$$

$$\hat{R}_{ii}^*(\xi) = \hat{u}'_i(\xi) \cdot \hat{u}'_i(\xi) , \quad (100)$$

where  $(\hat{\phantom{x}})$  denotes a Fourier transformed quantity,  $\xi$  is the spatial frequency and the superscript  $*$  implies the non-normalized correlation. Based on the Convolution theorem, the two-point correlation in the spectral space can be calculated by multiplying the Fourier transformed values with their conjugates. To obtain the normalized correlations in the physical space, the correlations in the spectral space need to be inverse Fourier transformed (`numpy.irfft`) back and then scaled with the one-point correlation, which is the value of the first element in the inverse Fourier transformed field. The present streamwise correlations were averaged in  $z$  direction and spanwise correlations in  $x$  direction as well as both correlations in time by including 25 uncorrelated time steps to make them less noisy.

Figures 17 and 18 show the two-point correlations in the  $x$ - and  $z$ -directions, respectively. From the figures it can be observed, that the majority of velocity correlations vanish, which suggests that the possible accumulating effects of periodicity are not significant. However, on the suction side there is a visible correlation left for  $u'$  very close to the wall, that explains the periodic behavior of the wall shear stress. This behavior is originating from the significantly elongated structures which cannot be fully captured even with a very long domain. Similar left-over correlations have been found in several numerical studies of a spanwise rotating channel flow, for example in the DNS study of Kristoffersen and Anderson [1]. The upward turn of the correlation plane indicates that the turbulent structures become more elongated towards the suction side, although after the peak they once more start to

shorten. This behavior suggests that the turbulence state near the wall is indeed semi-turbulent, comprising of a wide spectrum of meaningful length scales, and is in agreement with the wall shear stress patterns. On the pressure side, the turbulence length scales are generally small. As observed from the wall shear stress patterns, the system rotation was found to shorten the streaks and similar behavior was identified by Kristoffersen & Andersson who compared the correlations of a rotating and non-rotating channel.

In the spanwise direction, some left-over correlation of  $u'$  can be observed near the suction side. This is probably resulting from the inclined nature of the elongated structures. In the pressure side side graphs, a large negative correlation ‘cavity’ of  $R_{vv}$  that continues until the first third of the suction side is distinguished. This is a clear indicator of the roll cells, which tend to move towards pressure side with increasing rotation number. The spanwise length scale of these vortices was identified to be  $r_z/h = 0.68$ , which occurs at  $y/h \approx -0.3$ . The wall-normal length scale can approximated with the  $y$  distance where the correlations for  $v'v'$  vanish. The distance was found to be  $r_y/h \approx 1.4$  starting from  $y/h = -0.97$ .

The turbulence energy spectra were studied to provide information about Large Eddy simulation filter cut-off and also to provide reference data for WMLES simulations. The spectra also are only examined for the  $Ro = 0.45$  case, since the possible changes resulting to the wall-modeling should be distinguishable even by considering a single case. The streamwise turbulent kinetic energy  $E_{xx}$  in the spectral space can be calculated from the Fourier transformed fluctuations as

$$E_{xx}(k_x) = \frac{1}{2} \hat{u}^2, \quad (101)$$

The wavenumber in the streamwise direction is defined as

$$k_x = \frac{2\pi N}{L_x}, \quad (102)$$

where  $N$  is a streamwise cell index corresponding a single velocity point. The Energy spectra was only studied in the streamwise direction, and the results were made less noisy by averaging the Fourier transformed velocities in the  $z$ -direction and time.

Watmuff et al. [49] have studied the effects of system rotation on the streamwise turbulence energy spectrum through experimental research. Their primary observation was that the system rotation mainly modifies the energy of the largest scales by increasing it for the pressure side and decreasing for the suction side. This trend is also visible in the present simulation results, but not in the vicinity of the walls due to the significantly higher rotation rate. In the present study, the suction side undergoes a transition into semi-turbulent state, whereas Watmuff et al. used low rotation rates, where both sides remain completely turbulent.

Energy spectra at different local  $y^+$  values are presented in Figure 19. In the immediate vicinity of the walls, it can be seen that the turbulent kinetic energy is overall lower on the suction side than on the pressure due to the significant stabilization into quasi-turbulent state and the thickening of the viscous sublayer. When moving away from the wall, the trend of the rotation mainly affecting the large scales

can be observed, although the effect is opposite than Watmuff et al. had identified. The present simulation suggest that the streamwise turbulent kinetic energy is in fact increased at low wave numbers near the area of the elongated structures if the rotation is moderately high. The observation is in agreement with the correlation graphs, as they indicate the presence of the very long structures on the suction side. Furthermore, the energy levels of these large structures confirm that they are highly energetic structures, and the correlation values are not resulting from the normalization (a very small divided by a very small). Instantaneous  $u'$  velocity fluctuation field at  $y_s^+ = 40$  in Figure 20 visualizes these elongated structures. After this highly correlated area of elongated structures  $y^+ > 220$ , the spectra start behaving similarly as in the experimental results of Watmuff et al, and the energy of largest scales is decreased on the suction and increased on the pressure side. In the middle of the domain, the spectra naturally merge into each other. When considering the total turbulent kinetic energy  $E = \frac{1}{2}(\hat{u}'^2 + \hat{v}'^2 + \hat{w}'^2)$ , the rotation was found to globally decrease or increase the energy at especially at low wave numbers. Thus, it is possible to conclude that large modes of  $v'v'$  and  $w'w'$  are most affected by the system rotation.

Because of the LES cut-off, the smallest scales cannot be considered as absolute. Therefore, the differences in the smallest scales are most likely resulting from differences in resolution, as the suction side is known to be better resolved than the pressure side. Furthermore, there is a small amount of energy accumulation occurring at the smallest scales. This small peak in energy likely results from too low dissipation of the subgrid-scale model, and it has been encountered in the context of more advanced models. The effect could probably be reduced by using a more dissipative SGS model, such as Smagorinsky or significantly refining the mesh. However, the energy peak is very small compared to more energetic scales and similar levels of energy accumulation has been neglected in the literature [50].

It is also interesting to study length scales of the most energetic turbulence scales as a function of  $y$  in the whole domain. It provides good reference data in order to study whether or not the wall-model affects the dynamically most important structures in the outer layer. This procedure was done by thresholding the local largest 20 % of spectral density  $k_x E_{xx}$ , dividing them into equally spaced isocontours and visualizing them as a function of dimensionless wavelength in global wall units  $\lambda^+ = \frac{2\pi}{k} \frac{u_\tau \rho}{\mu}$  and  $y$ . Figure 21a presents these isocontours in the whole domain and the different stability zones can be distinguished in the figure. In the neutral zone, the most energetic turbulence scales are clearly constant. In the stabilized suction side boundary layer, these scales tend to become larger, since the moderate scales are more diminished than the largest scales as seen in Figure 19. The behavior of the destabilized pressure side is examined more closely in 21b in which the axes are scaled with pressure side friction velocity  $u_\tau^p$ . In this figure, the most energetic scales are nearly constant up to  $y^+ \approx 30$ , after which they tend to grow linearly in a logarithmic scale. The reason behind this phenomenon is the energy cascade principle, as the turbulent structures are yet to scatter into the smallest scales. The shape the destabilized region curve resembles the shape of the corresponding curve of non-rotating channel by Jimenez [33]. However, the length of the logarithmic

region clearly differs, since the self-similar logarithmic layer is modified, as also observed in the mean velocity graphs. In addition, the ‘universal’ region at  $y^+ < 30$  is slightly translated in  $\lambda^+$ , since the system rotation affects the local wall shear stress magnitudes.

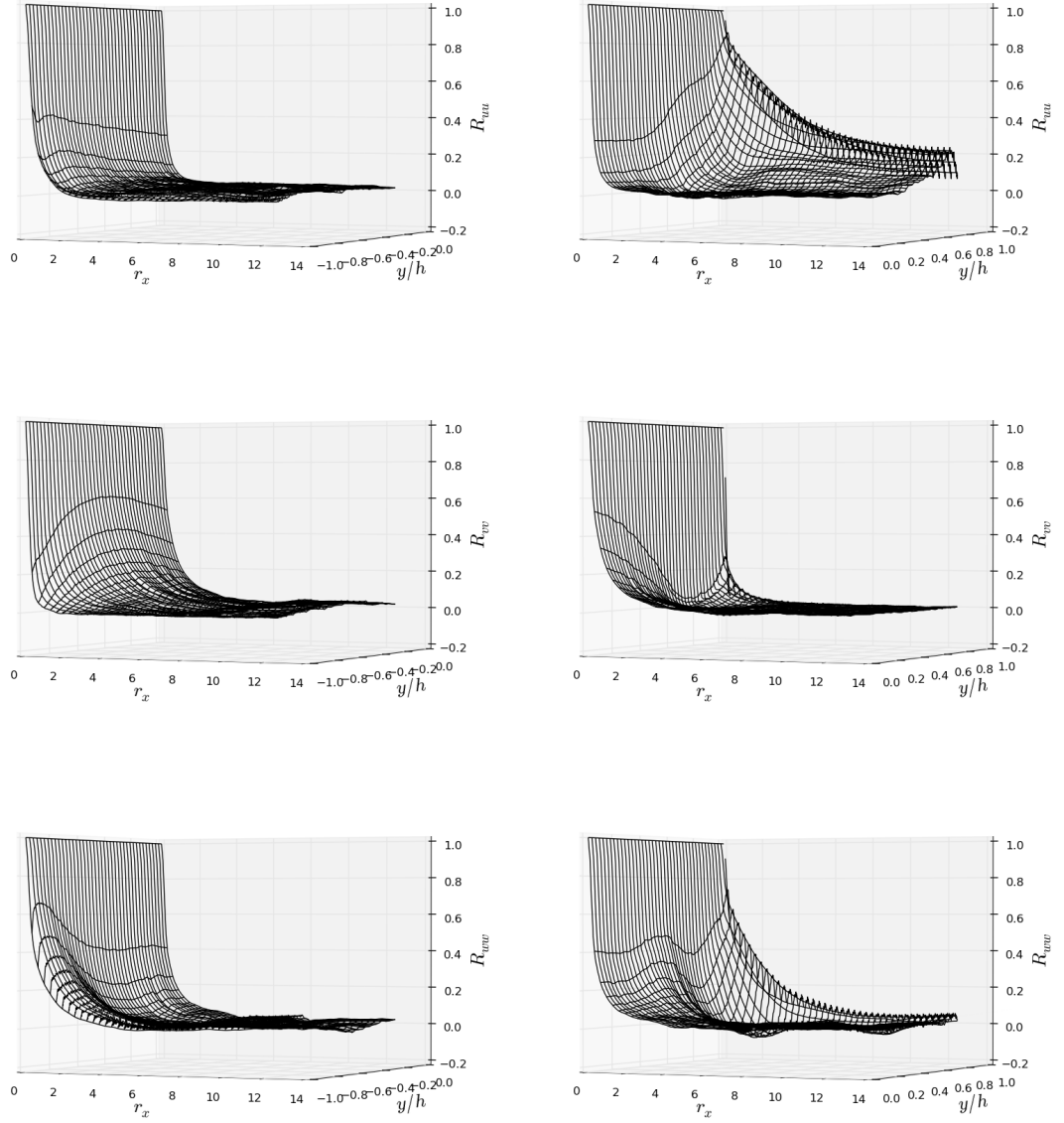


Figure 17: Streamwise two-point correlations for the velocity fluctuations as a function of the streamwise length scale and  $y$  for the  $Ro = 0.45$  case.

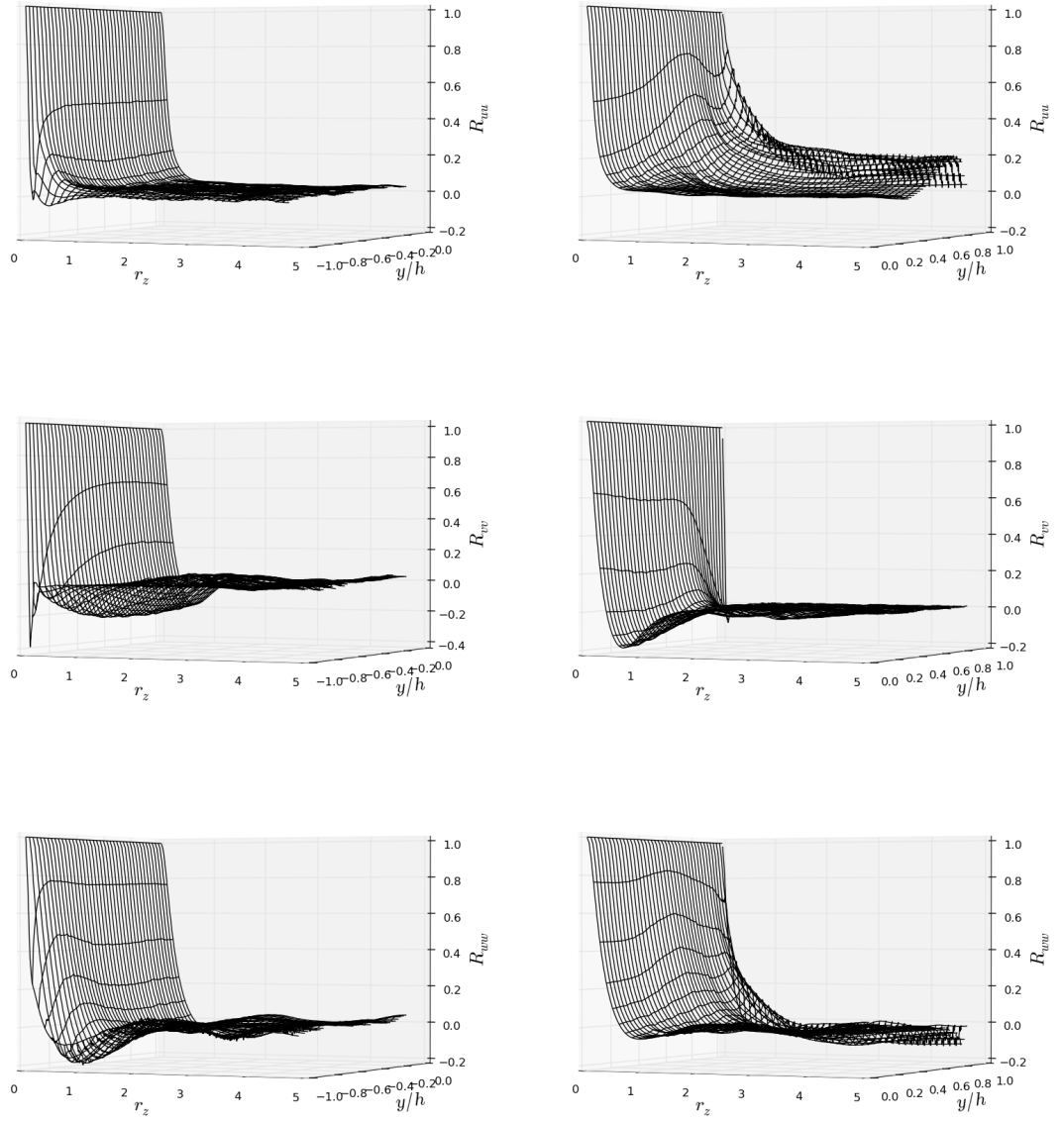


Figure 18: Spanwise two-point correlations for the velocity fluctuations as a function of the spanwise length scale and  $y$  for the  $Ro = 0.45$  case.

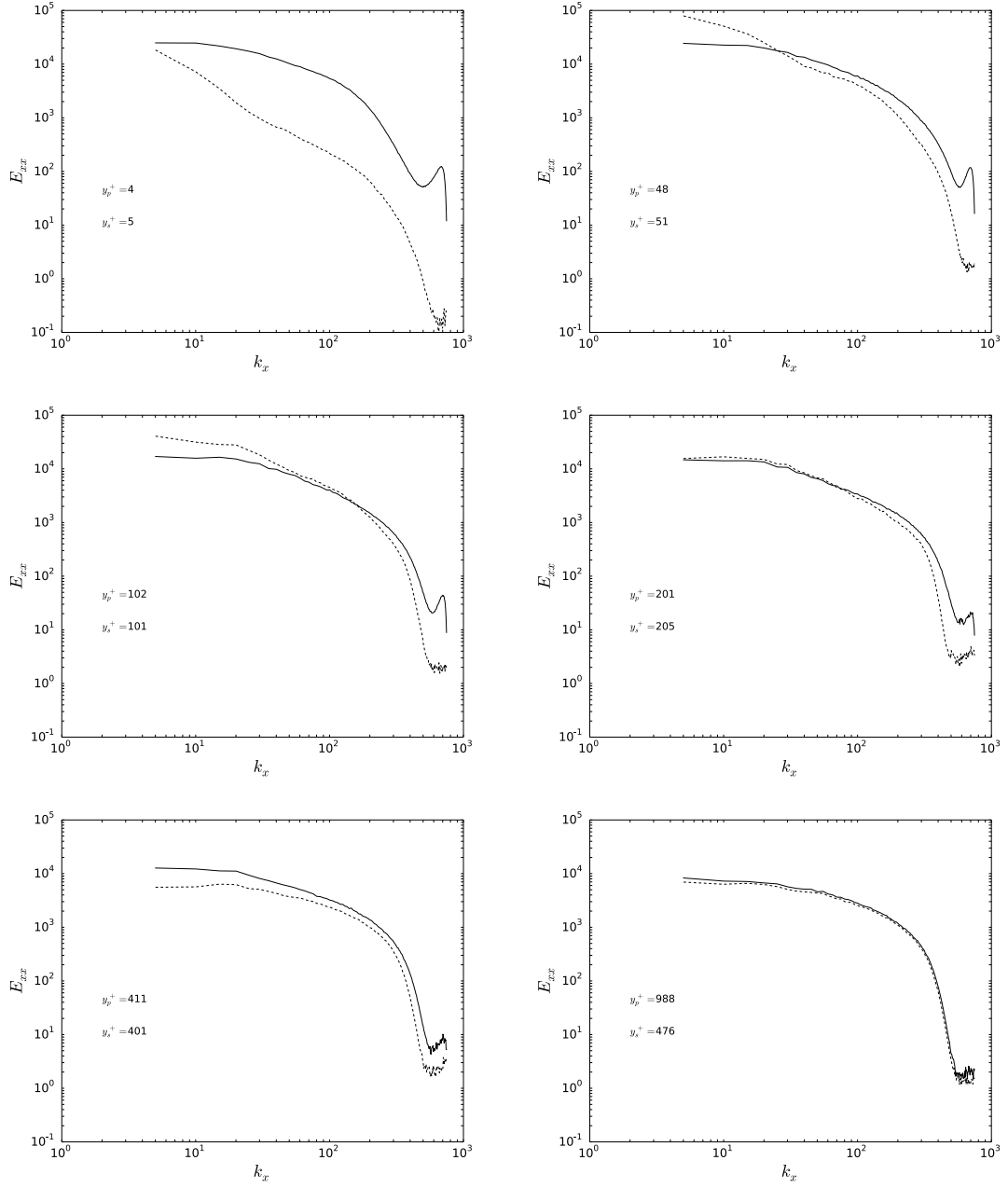


Figure 19: Turbulent kinetic energy spectra at different respective  $y^+$  values for the  $Ro = 0.45$  case. Pressure side —, suction side ---.

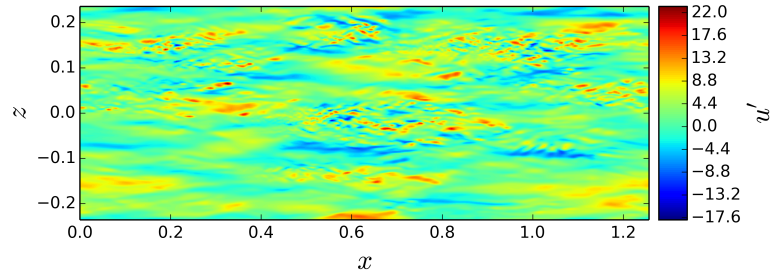


Figure 20: Elongated turbulent structures at  $y_s^+ = 40$  visualized with the instantaneous velocity fluctuation field.

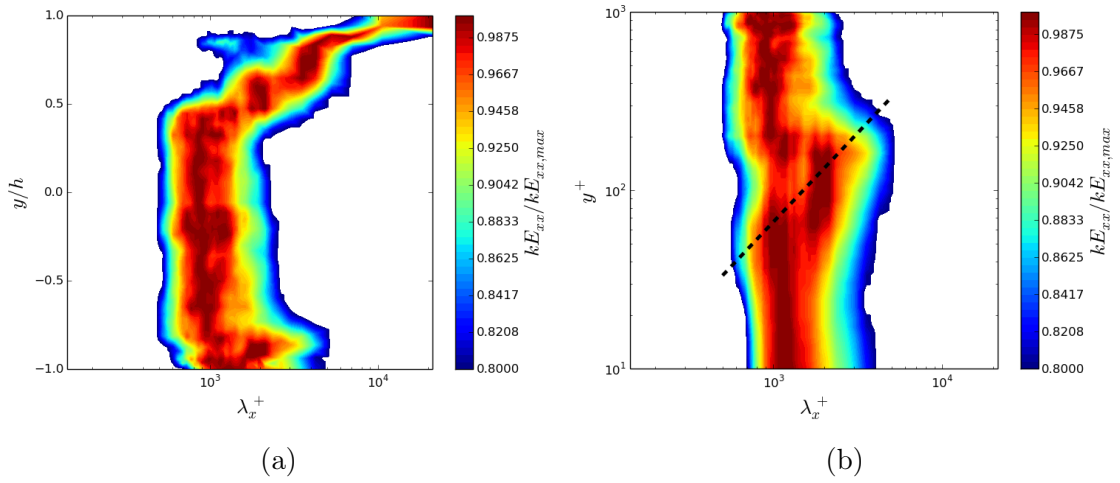


Figure 21: (a) Local spectral density of the turbulent kinetic energy  $k_x E_{xx}$  as a function of a length scale  $\lambda_x^+$  and dimensionless  $y$  coordinate for the  $Ro = 0.45$  case. Shaded isocontours represent the highest 20 % of the most energetic scales. (b) Local spectral density of  $k_x E_{xx}$  as a function of  $y_p^+$  for the pressure side.

## 7 Wall-Model for Charles<sup>X</sup>

### 7.1 Current Inner Layer Wall-Model

The current wall-modeling methodology implemented in the Charles<sup>X</sup> solver was proposed by Kawai & Larsson [2]. It is based on solving the equilibrium boundary layer equations in an embedded auxiliary grid, which is extruded from the wall. The auxiliary calculation is done in one dimension sequentially for each 'pillar' of cells within the wall-model layer, and only the viscous term is included in momentum the equation. Thereby, the momentum equation could be understood as a one-dimensional (viscous) diffusion equation for a scalar, which is the wall-parallel velocity. The energy equation representation is also one-dimensional and can be derived from the total energy equation with equilibrium assumptions [7]. The governing wall-model equations are defined as

$$\frac{d}{dy_w} \left[ (\mu + \mu_{\tau,wm}) \frac{du_{||}}{dy_w} \right] = 0 , \quad (103)$$

$$\frac{d}{dy_w} \left[ (\mu + \mu_{\tau,wm}) u_{||} \frac{du_{||}}{dy_w} + (\lambda + \lambda_{t,wm}) \frac{dT}{dy_w} \right] = 0 , \quad (104)$$

where  $\mu_t$  denotes the turbulent viscosity,  $u_{||}$  denotes the wall-parallel velocity,  $y_w$  is the coordinate normal to the wall, and  $\lambda$  is the thermal conductivity. In the present wall-model, the turbulent viscosity is calculated by a simple mixing length model, which is defined as

$$\mu_t = \kappa \rho y \sqrt{\frac{\tau_w}{\rho}} D , \quad (105)$$

$$D = (1 - e^{-y_w^+/A^+})^2 , \quad (106)$$

where  $\kappa$  is the von Kármán constant  $\kappa = 0.41$ , and  $A^+$  is a case specific van Driest damping constant describing the dimensionless thickness of the viscous sublayer, for which Kawai and Larsson used a value  $A^+ = 17$ . The mixing length model produces values of turbulent viscosity based on the logarithmic velocity profile. Since the standard logarithmic velocity profile is forced within the embedded grid, the calculation of the wall shear stress is completely unaffected by the system rotation. This was found be the main disadvantage for applying this model for rotating flows and the baseline for further improvement.

The main difference of the methodology by Kawai & Larsson compared to traditional auxiliary grid methods is the placement of the auxiliary grid, which is no longer confined within the first off-wall LES cell. Thereby, in this methodology the input velocity and temperature are not taken from the first off-wall cell, where LES is necessary underresolved, but from a grid-independent location, which will be referred to as the exchange location. By overlapping few cells of the LES grid with the auxiliary wall-model grid, it is possible to obtain better estimation for the wall shear stress as the inputs are taken from a better resolved area. The authors suggested that the exchange location should be chosen from the log-layer in a manner

that there are at least four LES cells within the wall-model layer. After taking the input velocity and temperature as boundary conditions at the exchange location, the equilibrium equations are calculated with FVM in the auxiliary grid to obtain the wall shear stress and heat flux at the wall. Finally, these values are input to the LES calculation as boundary fluxes to update the first values of the off-wall LES cells. A schematic of this process is illustrated in Figure 22.

Since Charles<sup>X</sup> solver also supports unstructured grid topology, the grid independence of the exchange location is a necessary feature, since the extruded and structured auxiliary grid cannot be matched perfectly with the LES grid for complex geometries. Therefore, an interpolation procedure has to be introduced to obtain velocities at the exchange location, and it is done with a simple first order Taylor expansion

$$u_i^{EL} = u_i^{fa} + \frac{\partial u_i}{\partial x_j} (x_j^{EL} - x_j^{fa}) , \quad (107)$$

in which the superscripts *EL* and *fa* refer to the values at the exchange location and at the face center closest to the exchange location, respectively. Furthermore, the wall shear stress is assumed to be aligned to the interpolated velocity vector at the exchange location. [41]

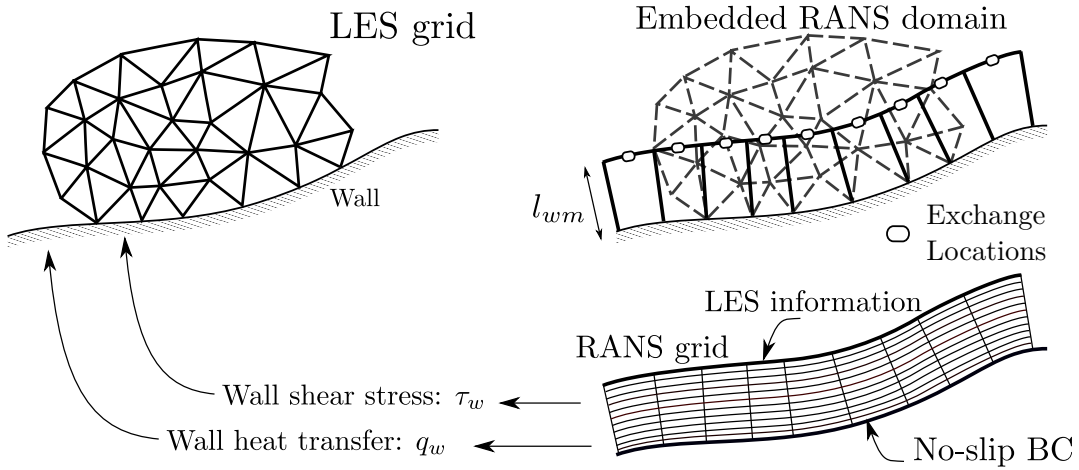


Figure 22: A schematic illustration of the auxiliary grid wall-modeling approach found in Charles<sup>X</sup> [41].

## 7.2 Rotation Corrected Wall-Model

As observed from the wall-resolved results, the system rotation essentially modifies the logarithmic velocity profile, which causes the standard mixing length turbulence model to be unfeasible. Several studies, such as the work by Howard et al. [51], have been performed to study the rotation corrected mixing length model as part of general turbulence modeling in RANS framework. As most of the RANS turbulence models tend to reduce to the mixing length model near the wall, applying a similar methodology for wall-modeling in LES framework is now proposed. The principle

idea is to change the standard mixing length turbulence model in the present wall-model to adapt to the stabilizing and destabilizing effects of the Coriolis force by locally decreasing and increasing the value of turbulent viscosity. The approach is logical, since the Coriolis acceleration only affects the main flow through the turbulence as discussed in Chapter 4. In other words, by increasing and decreasing the turbulent viscosity in destabilized and stabilized regions, it is possible to modify the forced velocity profile in the auxiliary grid to mimic the real velocity profile.

The modified mixing length was first introduced by Bradshaw [11] and it is a function of the local stability parameter, the gradient Richardson number. Several different formulations of the mixing length model and the correction have been proposed, but they all have a common coefficient defined as

$$\frac{l}{l_0} = (1 - \beta Ri)^\alpha , \quad (108)$$

where  $l_0$  is the corresponding non-rotating mixing length, and  $\beta$  is a constant, which value varies between different studies and is dependent on the chosen exponent  $\alpha$ . By substituting the mixing length to the expression of turbulent viscosity, a rotation modified mixing length model is obtained to be a form of

$$\mu_t = (1 - \beta Ri)^\alpha \kappa \rho y_w \sqrt{\frac{\tau_w}{\rho}} D , \quad (109)$$

$$D = (1 - e^{-y_w^+/A^+})^2 , \quad (110)$$

$$Ri = S(S + 1) , \quad (111)$$

$$S = -\frac{2\Omega}{(\partial u_{||}/\partial y_w)} . \quad (112)$$

As seen in Equation (112), the model is now dependent on the rotation rate and thus also on the rotation number.

### 7.3 Stand-Alone Wall-Model Algorithm

A stand-alone wall-model with the rotation correction option was implemented in a separate python program using FVM to provide a quick testing tool for the *a priori* wall-model analysis. Only the momentum equation was considered, since the simulations were done in the incompressible flow regime without heat transfer. Furthermore, from the Navier-Stokes equations it can be seen that rotation does not directly affect the energy equation. The auxiliary grid in the stand-alone wall-model is determined by user defined parameters, which are the exchange location (wall-model height), the numbers of cells and a stretching coefficient of two subsequent cells. The structure of the stand-alone wall-model algorithm with governing equations are presented next.

Let us start from the wall-model Equation (103), which gives a steady-state boundary value problem to calculate the wall shear stress. The equation is elliptic,

meaning that a disturbance at an arbitrary point would immediately affect all other points, and thus it needs to be solved by considering the entire domain simultaneously. Equation (103) can be integrated over a control volume, and by utilizing the Gauss' divergence theorem

$$\int_s \vec{f}(\phi) \cdot d\vec{S} = - \int_v \nabla \cdot \vec{f}(\phi) dV \quad (113)$$

it is possible to express the volume integral as a surface integral. By expressing the surface integrals discretely, Equation (103) can be written as

$$\sum_n \vec{f}(u_{||,j}) \cdot \vec{n}_j \Delta S_j = 0, \quad (114)$$

where  $\vec{f}(u_{||,j})$  is the flux density through one surface of a control volume  $j$ ,  $\vec{n}$  is the normal vector of the cell surface, and  $\Delta S_j$  is the area of the cell surface, which we from now on refer to as  $S_j$ . Since the wall-model is applied only in the wall-normal direction  $\vec{n}$  is either positive or negative  $y_w$  direction. Therefore, Equation (114) can be written in a more compact form with volume fluxes as

$$-F_{j+1/2} + F_{j-1/2} = 0, \quad (115)$$

where the volume flux is

$$F_{j+1/2} = f_{j+1/2} \cdot S_{j+1/2}. \quad (116)$$

According to the Gauss' theorem, the expression of the flux density can be found under the  $\nabla$  operator in the original Equation (103). Thus, the Volume flux at the surface  $S_{j+1/2}$  can be expressed as

$$F = (\mu + \mu_t)_{j+1/2} \frac{du_{||,j+1/2}}{dy_w} S_{j+1/2}. \quad (117)$$

The derivative can be approximated with the second order accurate centered scheme as

$$\left. \frac{du_{||,j}}{dy_w} \right|_{j+1/2} = \frac{u_{||,j+1} - u_{||,j}}{y_{w,j+1} - y_{w,j}}. \quad (118)$$

The eddy viscosity is calculated from the mixing length model (109) with the wall shear stress obtained in the previous iteration round. In the first round, an initial guess  $\tau_w = \mu \frac{u_{||,LES}}{y_{w,jmax+1}}$  can be used. The velocity gradient for the gradient Richardson number parameter  $S$  is calculated with the central difference scheme similarly as for the viscous flux. Furthermore, it is necessary to add an *ad hoc* type of limitation for the gradient Richardson number, since in the beginning of the iteration the gradients are zero or close, which causes the parameter  $S$  to become extremely large and  $Ri$  to have unrealistic values. For the suction side, the gradient Richardson number also needs to be limited to prevent the production of negative turbulent viscosity.

By substituting the expression of the volume flux to Equation (115) and grouping the terms for different velocities resulting from the discrete differentiation, the following form is obtained

$$\begin{aligned}
& - \frac{(\mu + \mu_t)_{j+1/2}}{(y_{w,j+1} - y_{w,j})} u_{||,j+1} \\
& + \left[ \frac{(\mu + \mu_t)_{j+1/2}}{(y_{w,j+1} - y_{w,j})} + \frac{(\mu + \mu_t)_{j-1/2}}{(y_{w,j} - y_{w,j-1})} \right] u_{||,j} \\
& - \frac{(\mu + \mu_t)_{j-1/2}}{(y_{w,j} - y_{w,j-1})} u_{||,j-1} = 0 .
\end{aligned} \tag{119}$$

The equation above can be expressed as a matrix equation  $A\vec{u} = \vec{d}$ , where the vector  $\vec{u}_{||}$  contains the velocity values for all nodes  $0 \dots jmax + 1$ . The indices 0 and  $jmax + 1$  refer to ghost cells, which are used to evoke the boundary conditions. The tridiagonal matrix  $A$  contains the corresponding coefficient values from Equation (119) and  $\vec{d}$  is a zero vector excluding the boundary condition values for the ghost cells. The indexing follows the convention of Python arrays, which start from zero.

The no-slip condition at  $j = 1 - 1/2$  can be set by mirroring the velocity value of the first true cell and the ghost cell. This can be implemented by setting the matrix coefficients  $A_{00} = 1$  (ghost) and  $A_{01} = 1$ , which leads to  $u_{||,0} + u_{||,1} = 0$ . The constant velocity at the exchange location can be defined similarly by setting the coefficients  $A_{jmax+1,jmax+1}$  and  $A_{jmax+1,jmax}$  to unity and the right-hand side to  $d_{jmax+1} = 2u_{||,LES}$ . This essentially leads to defining the velocity at the border of the domain to be  $\frac{1}{2}(u_{||,jmax} + u_{||,jmax+1}) = u_{||,LES}$ .

Since the coefficient matrix  $A$  is tridiagonal, the system of equations can be directly solved by Thomas algorithm. In the context of Thomas algorithm, let us denote the lower, main and upper diagonal with  $\vec{a}$ ,  $\vec{b}$  and  $\vec{c}$ , respectively. The Thomas algorithm comprises of two parts, the forward sweep and backward substitution. In the first phase the coefficient matrix is manipulated into a form, where  $\vec{a}$  is eliminated,  $\vec{b}$  is normalized to produce unity and  $\vec{c}$  and  $\vec{d}$  are modified as

$$c'_j = \begin{cases} \frac{c_0}{b_0} & \text{when } j = 0 \\ \frac{c_j}{b_j - a_j c'_{j-1}} & \text{when } j = 1 \dots jmax + 1 , \end{cases} \tag{120}$$

$$d'_j = \begin{cases} \frac{d_0}{b_0} & \text{when } j = 0 \\ \frac{d_j - a_j d'_{j-1}}{b_j - a_j c'_{j-1}} & \text{when } j = 1 \dots jmax + 1 . \end{cases} \tag{121}$$

In the backward substitution phase, the  $\vec{u}_{||}$  values are obtained from the forward sweep modified matrix with the relations

$$u_j = \begin{cases} d'_{jmax+1} & \text{when } j = jmax + 1 \\ d'_j - u_{j+1} & \text{when } j = jmax + 1 \dots 0 . \end{cases} \tag{122}$$

The Thomas algorithm produces the exact solution for the system of equations and the wall shear stress can be calculated by

$$\tau_w = \mu \frac{u_{||,1}}{y_{w,1}} \tag{123}$$

However, since the matrix coefficients are dependent on the turbulent viscosity, which is coupled to the wall calculated wall shear stress, this entire process needs to be repeated until the solution has converged. The convergence criterion used in the *a priori* analysis was that the difference in  $L^2$ -norm of  $\vec{u}_{||}$  between two sequential iteration rounds is below  $1 \cdot 10^{-6}$ , which takes less than 10 iteration rounds.

## 7.4 *A Priori* Testing Methodology

The *a priori* testing in the context of wall-modeling is a term for an approach, where a stand-alone wall-model is applied to wall-resolved results. It is a quick method to examine wall-models and see how different modifications affect the calculated wall shear stress and the wall-model velocity profile. The *a priori* analysis is typically done only for average quantities by taking the input exchange velocity from the statistical mean profile to obtain the estimation for the mean wall shear stress. However, since the wall-model in true wall-modeled simulations always uses the instantaneous velocities, having the averages to match with this method might be misleading because of non-linearities. Therefore, in addition to studying the average quantities, the statistics of the instantaneous wall shear stresses are examined by applying the model to every cell on the exchange plane and several time steps. With this method, it is possible to investigate the distribution of different wall shear stress magnitudes as well as their direction through the joint probability density function. This approach also provides insight, whether or not it is sufficient to investigate the mean shear stress by taking the mean velocity as an input.

## 7.5 *A Priori* Testing Results

### 7.5.1 Mean Quantities

Figures 23, 24 and 25 show the average velocity profiles calculated with the *a priori* stand-alone wall-model for the different Rotation numbers with and without the rotation correction. The wall-resolved results are visualized in the graphs for comparison, and the exchange velocities for the wall-model were taken from these mean velocity profiles. The wall-model velocity profiles are scaled with the shear velocity resulting from the model, as the wall-resolved profiles are scaled with the true wall shear stress. Thus, the differences in wall shear stresses can be seen in the differences of  $\bar{U}^+$  values at the exchange location (the end of the wall-model curves). Different curves in each graph represent different values of van Driest damping constant  $A^+$  and they need to be chosen adequately and given as an input for both sides in each case, since the system rotation locally changes the thickness of the viscous sublayer. The parameters in the rotation correction  $(1 - \beta Ri)^\alpha$  were chosen as  $\beta = 3.6$  and  $\alpha = 1$ , based on manually testing different combinations found in the literature.

The first observation in all of the graphs is the significance of the van Driest damping constant  $A^+$ . With or without the rotation correction, the optimal selection of  $A^+$  will produce almost a perfect prediction for the wall shear stress on the pressure side. However, in each case, the rotation corrected model clearly finds the

correct slope of the logarithmic profile slope significantly better than the standard model, which indicates that it is less dependent on the exchange location. This was proven to be true by studying the error in the wall shear stress with different  $A^+$  and exchange location combinations. The error graphs for the case  $Ro = 0.45$  in Figure 26 show us that the rotation corrected model is almost independent on exchange location while the standard model requires the optimum combination of both parameters. The same trend was identified in the two other cases as well. Although with  $Ro = 1.2$  the profile slope becomes remarkably shorter, and thus limits the correct interval for the exchange location. Nevertheless, the necessity of the rotation correction also increases with increasing  $Ro$ , as the deviation from the standard logarithmic profile slope becomes larger. The independence on the exchange location is a highly desirable feature for WMLES, which causes  $A^+$  to behave only as an offset to take into account the change in the viscous sublayer thickness. This behavior is exceptionally important for the current wall-model implementation in Charles<sup>X</sup>, since the exchange location can be chosen grid independently.

For the suction side, the trends are similar and the rotation correction tends to turn the curves towards the correct profile, although there are no clear logarithmic slopes especially with the higher two rotation numbers. The shapes of the wall-model profiles now indicate that the error tends to grow with increasing exchange location especially for high rotation numbers. This behavior naturally excludes high exchange locations especially for high rotation rates. The rotation corrected wall-model for with  $Ro = 1.2$  behaves uniquely on the suction side, since the rotation correction completely suppresses the turbulent viscosity, as seen in Figure 22b. This is not a problematic feature, since it only occurs at high  $Ro$  when the correct profile is anyhow very close to fully laminar.

The optimal values for the van Driest damping constant  $A^+$  behave as expected, and their integer values with corresponding relative wall shear stress errors are gathered in Table 2. The clear trend is that the value  $A^+$  needs to be increased for the suction and decreased for the pressure side because the system rotation increases and decreases the height of the viscous sublayer respectively. Since stability effects are proportional to the combination of  $Ro$  and  $Re$ , proposing an empirical correlation is difficult, as it would have to be a function of both numbers.

$Ro$	$A_p^+$	$A_s^+$	$\tau_{w,RC}^p/\tau_w^p$	$\tau_{w,eq}/\tau_w^p$	$\tau_{w,RC}^s/\tau_w^s$	$\tau_{w,eq}/\tau_w^s$
0.15	15	32	1.00	0.94	1.00	1.06
0.45	11	50	0.99	0.87	1.02	1.06
1.2	8	50	0.99	0.85	0.96	1.07

Table 2: Summary of the *a priori* test results. Subscripts and superscripts  $p$  and  $s$  denote pressure and suction side respectively. The subscript  $RC$  refers to the rotation corrected wall-model and  $eq$  to the standard equilibrium model.

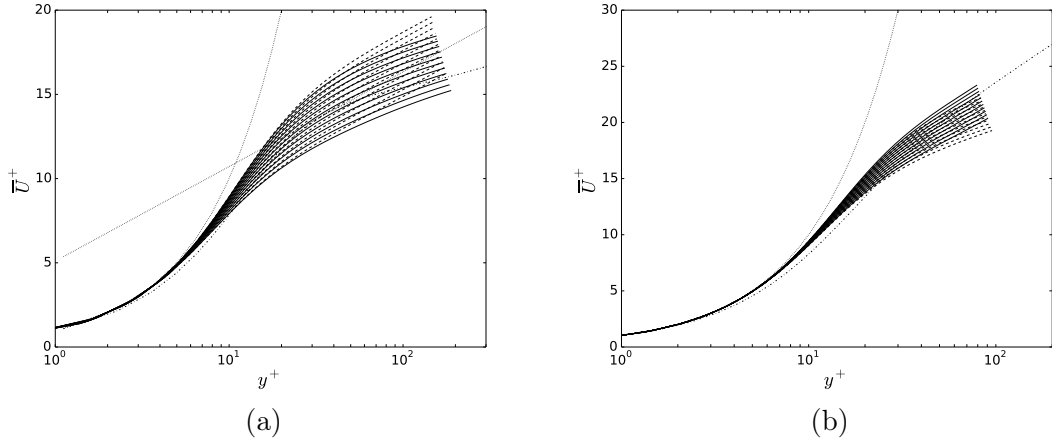


Figure 23: *A priori* wall-modeled velocity profiles when  $Re = 20\,000$  and  $Ro = 0.15$ . Rotation corrected wall-model —, standard wall-model ---, wall-resolved -·-, standard logarithmic velocity profile and laminar profile ·····. (a) Pressure side when van Driest damping constant  $A^+ = 13 - 23$ . (b) Suction side when  $A^+ = 25 - 35$ .

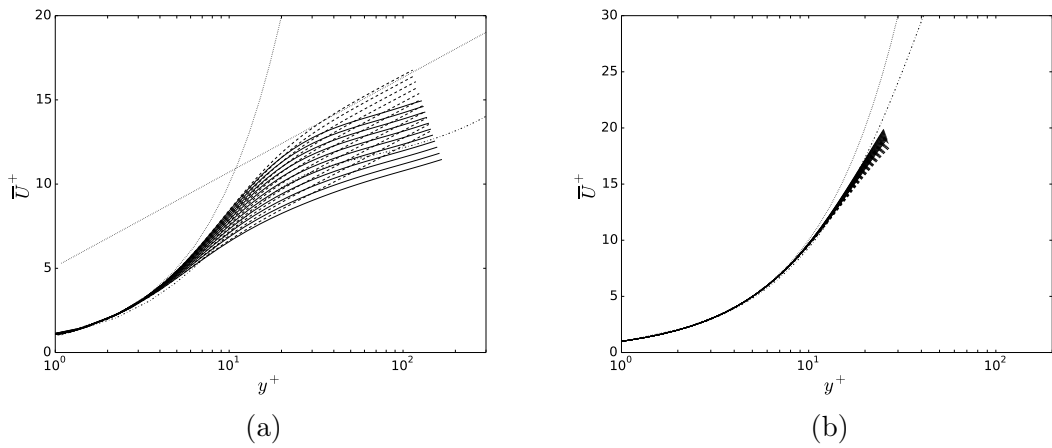


Figure 24: *A priori* wall-modeled velocity profiles when  $Re = 20\,000$  and  $Ro = 0.45$ . Rotation corrected wall-model —, standard wall-model ---, wall-resolved -·-, standard logarithmic velocity profile and laminar profile ·····. (a) Pressure side when van Driest damping constant  $A^+ = 7 - 17$ . (b) Suction side when  $A^+ = 40 - 50$ .

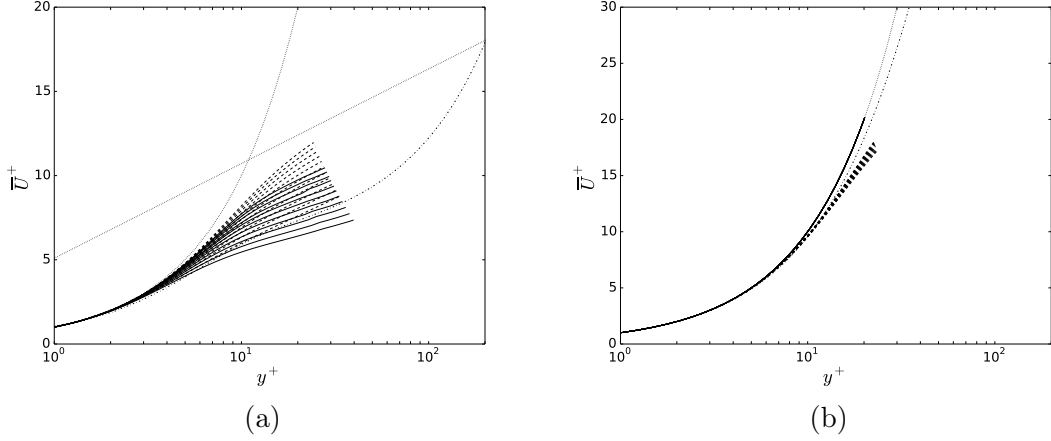


Figure 25: *A priori* wall-modeled velocity profiles when  $Re = 20\,000$  and  $Ro = 1.2$ . Rotation corrected wall-model —, standard wall-model ---, wall-resolved - · -, standard logarithmic velocity profile and laminar profile ····. (a) Pressure side when van Driest damping constant  $A^+ = 5 - 15$ . (b) Suction side when  $A^+ = 40 - 50$ .

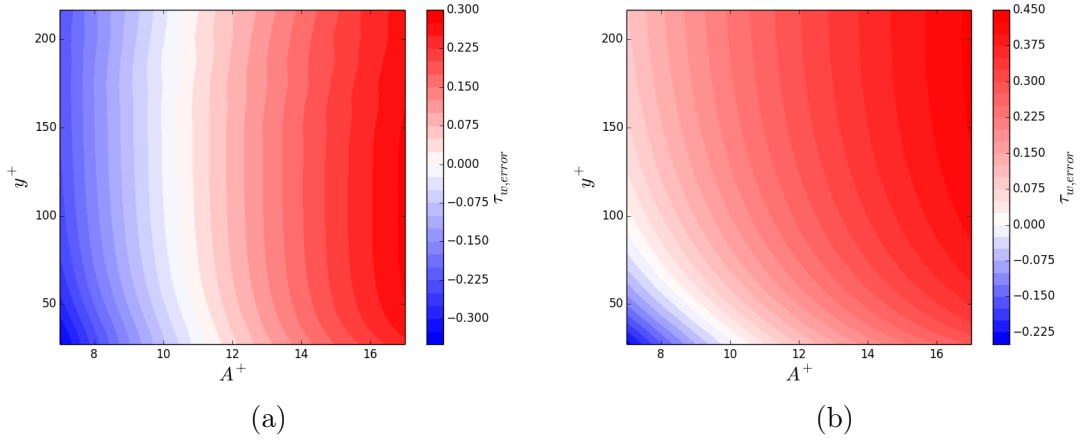


Figure 26: The relative error in the wall shear stress magnitude compared to the wall-resolved value as a function of van Driest damping constant  $A^+$  and the exchange location. (a) Rotation corrected wall-model (b) Standard wall-model.

### 7.5.2 Instantaneous Statistics

Instantaneous wall shear stress statistics were investigated by the joint probability density function. The joint probability density function fulfills the conditions

$$Pr(\theta_1 \leq \theta \leq \theta_2, \tau_{w1} \leq \tau_w \leq \tau_{w2}) = \int_{\theta_1}^{\theta_2} \int_{\tau_{w1}}^{\tau_{w2}} f_{\theta}(\theta) f_{\tau_w}(\tau_w) d\theta d\tau, \quad (124)$$

$$\int_{\theta_{min}}^{\theta_{max}} \int_{\tau_{wmin}}^{\tau_{wmax}} f_{\theta}(\theta) f_{\tau_w}(\tau_w) d\theta d\tau = 1, \quad (125)$$

where  $Pr$  is the probability,  $\theta$  is the wall shear stress angle and  $f_{\tau_w}$  and  $f_{\theta}$  denote the probability density functions for the wall shear stress and its angle, respectively. Discrete probability density functions can be calculated using the *2Dhistogram* function found in Python's Numpy library.

Joint probability density study based on the magnitudes and angles of instantaneous wall shear stresses was performed for the  $Ro = 0.45$  case. The input velocities were taken from 25 uncorrelated exchange location planes at  $y^+ \approx 45$  for the pressure and  $y^+ \approx 20$  for the suction side. The *a priori* testing algorithm was applied to each cell on these planes, providing us statistics of over 2.6 million individual *a priori* analyses. The rotation correction was switched on and  $A^+$  was chosen to be 11 for the pressure and 50 for the suction side.

Figures 27 and 28 show graphs of the joint probability density on the pressure side and suction side, respectively. From these graphs it can be seen that, wall-modeling seems to significantly change the statistical distribution of instantaneous wall shear stresses. In terms of magnitude, the changes are not drastic, but surprising is that the wall-model seems to increase the maximum and minimum values compared to the wall-resolved results on the pressure side. This observation suggests that the wall-model actually overestimates the highest and underestimates the lowest instantaneous wall shear stresses, while still keeping the average approximately the same. The significant filtering of the wall-modeled wall shear stress angles was completely expected, since the angles are defined by the velocity orientation at the exchange location. As the exchange location is further away from the wall, where the  $u$ -velocity component is always more dominant than  $w$ , the variation in terms of angles becomes smaller. This effect was found to be even more prominent on the suction side.

Statistical studies for the instantaneous wall shear stress were not performed for the other two rotation case, as they are expected to behave similarly. Furthermore, these probability tests suggest that the average wall shear stress can be estimated by directly examining the mean values, since they produce the probability peak very close to the correct wall shear stress value.

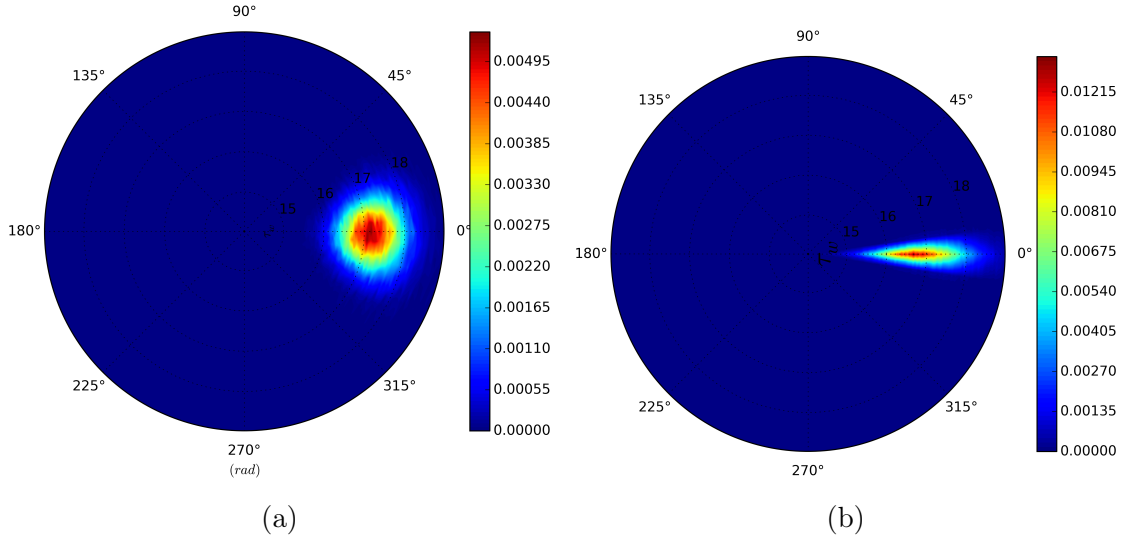


Figure 27: Probability densities for the wall shear stress magnitude and angle on the pressure side when  $Ro = 0.45$ . (a) Wall-resolved (b) *A priori* wall-modeled.

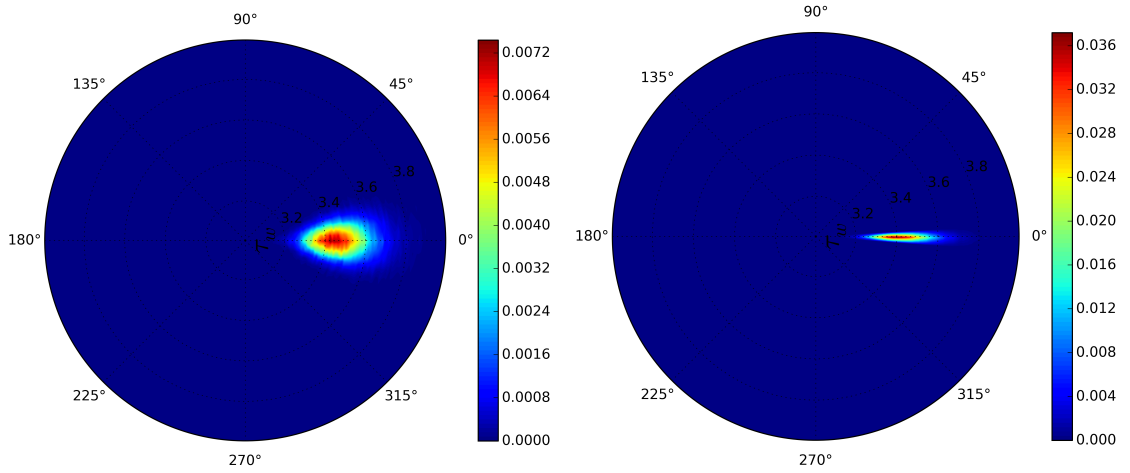


Figure 28: Probability densities for the wall shear stress magnitude and angle on the suction side when  $Ro = 0.45$ . (a) Wall-resolved (b) *A priori* wall-modeled.

## 8 Wall-Modeled Large Eddy Simulation

After establishing the rotation correction principle to be feasible through *a priori* testing, it was implemented into the Charles<sup>X</sup> solver. Wall-Modeled Large Eddy Simulations were then performed to investigate if the promising behavior observed in the analysis is still maintained when the wall-model works as part of the simulation. Although the *a priori* testing is a good approach to have preliminary guidance about the wall-model, it cannot predict failures due to robustness or coupling effects. Since the wall-modeled wall shear stress defines the velocity at the first off-wall grid point, it has an indirect effect to the exchange velocity as well. Therefore, it is possible that the modeling errors accumulate compared to the *a priori* predictions, although utilizing several true LES cells within the wall-modeling zone should make it less significant. Furthermore, with the WMLES data it is also possible to study the changes in the flow field dynamics.

### 8.1 Setup

Wall-Modeled Large Eddy simulations were performed with a similar setup as the wall-resolved simulations. The same amount of grid points were used in the stream-wise and spanwise directions, but the number of grid points in the  $y$ -direction was decreased to from 100 to 70 resulting in 315 000 total decrease in LES control volumes. The exchange location was fixed at  $y_0/h = 0.04$  for both sides, and four LES cells were placed within this region. In wall units, the exchange location was found to be at  $y^+ = 45$  for the unstable, and  $y^+ = 20$  for the stable side. Although four LES cell was placed to overlap the wall-model region, the first LES cell height was seven times larger than in the wall-resolved case. This provides a significant advantage in terms of the time step, which is constrained by the Courant–Friedrichs–Lewy *CFL* condition, since explicit time integration was used. The *CFL* condition is proportional to dimensions of the smallest cell as

$$C = \frac{u \Delta t}{\Delta x} + \frac{v \Delta t}{\Delta y} + \frac{w \Delta t}{\Delta z} < C_{max}. \quad (126)$$

The seven times larger cell height was found to produce approximately a seven times larger time step. The number auxiliary grid cells in the wall-normal direction was chosen to be 30 for both sides. Although these auxiliary cells in fact increased the number of total cells (LES + WM), due to the simplicity of the wall-model equations, which were found to converge in approximately three iterations, the simulation could theoretically lead up to ten times cheaper simulation based on the combination of total LES cells and the appropriate timestep,  $\frac{10.5M \times 7}{7.35M} = 10$ . In order to get a proper idea about the quicker flow development and convergence, the initial velocity field was interpolated from the same three million cell result as the wall-resolved simulations, not from the converged wall-resolved field. Only the  $Ro = 0.45$  case was performed as wall-modeled, as it should be sufficient to find problematic behaviors by considering only one case. Nevertheless, an underresolved simulation, which utilizes the WMLES grid without the wall-model, was performed to investigate the necessity of the wall-modeling.

As the converged wall-resolved simulation required around 320 000 CPUh, the wall-modeled simulation was found to be converged in around 80 000 CPUh. The preliminary estimate of ten times faster was clearly overestimated, as the auxiliary grid computation time was neglected. Furthermore, additional slowdown can occur if the partitioning is not optimized for the wall-model, since the partitions containing many wall cells become more demanding due to the auxiliary wall-model computation. This can lead to bottlenecks in message passing and MPI barriers, and thereby it is reasonable to use dual-constraint partitioning. The dual-constraint partitioning algorithm evens the number of wall-model cells for each partition with a certain given threshold, for example allowing 2% difference. In the current simulation, a threshold value of 1% was used.

## 8.2 Results

The mean velocity profiles in the outer layer scaling and in wall units are shown in Figure 29. The wall-resolved and underresolved simulation results are also visualized in the graphs as a reference. From the results, it can be seen that the wall-modeled simulation very well predicts the shape of the mean profile despite the small deviation near the suction side. Also the velocity profiles in wall units are in very good agreement with the wall-resolved results beginning from the exchange location. The overlapping LES cells within the wall-model region should not be included in the results, since they do not properly capture the turbulence physics due to the low resolution. The underresolved simulation also produces surprisingly good results on the stable side. This behavior suggests that even the coarser wall-model grid seems to provide sufficient resolution for the inner layer, as the viscous sublayer is extended by the stabilizing effect of the Coriolis force. Therefore, for high rotation rates when the flow is surely expected to be very close to laminarization on the stable side, it might be a feasible approach to disable the wall-model, since the exchange location needs to be anyhow defined very close to the wall. On the pressure side, underresolving the viscous sublayer produces approximately 9% overprediction for the wall shear stress compared to the 0.7% error resulting from the wall-model. This advocates the necessity of wall-modeling on the pressure side. Naturally, if the wall-model thickness would be increased and less overlapping cell placed within the wall-model region, the necessity of the wall-model would even further increase.

Figure 30 presents the Reynolds stresses of the wall-modeled simulation. Wall-modeled results are mainly in good agreement with the wall-resolved results, despite the notable underprediction of the streamwise Reynolds stress  $\overline{u'u'}$  near the pressure side. This underestimation is associated with the fact that the flow is underresolved within the first LES cells. The reason why this spike in the underresolved simulation is slightly better is due to the increased shear production resulting from the overestimation of the wall shear stress. The results for Reynolds stresses  $\overline{v'v'}$  and  $\overline{w'w'}$  are in good agreement in the whole domain. The trend of the wall-model clearly improving the results compared to the underresolved simulation can also be identified. Again, the differences are expected to become remarkably larger, if the wall-model height and the grid would not be chosen as conservatively.

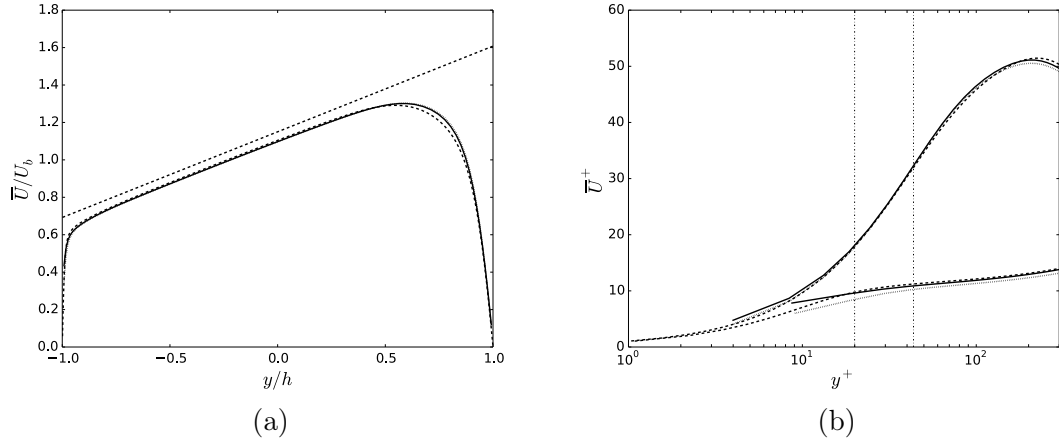


Figure 29: WMLES —, wall-resolved LES ---, under-resolved LES ····, exchange locations vertical ····.  $Re \approx 20\,000$  and  $Ro = 0.45$  (a) Mean velocity profiles in the outer layer scaling. (b) Mean velocity profiles in respective wall units.

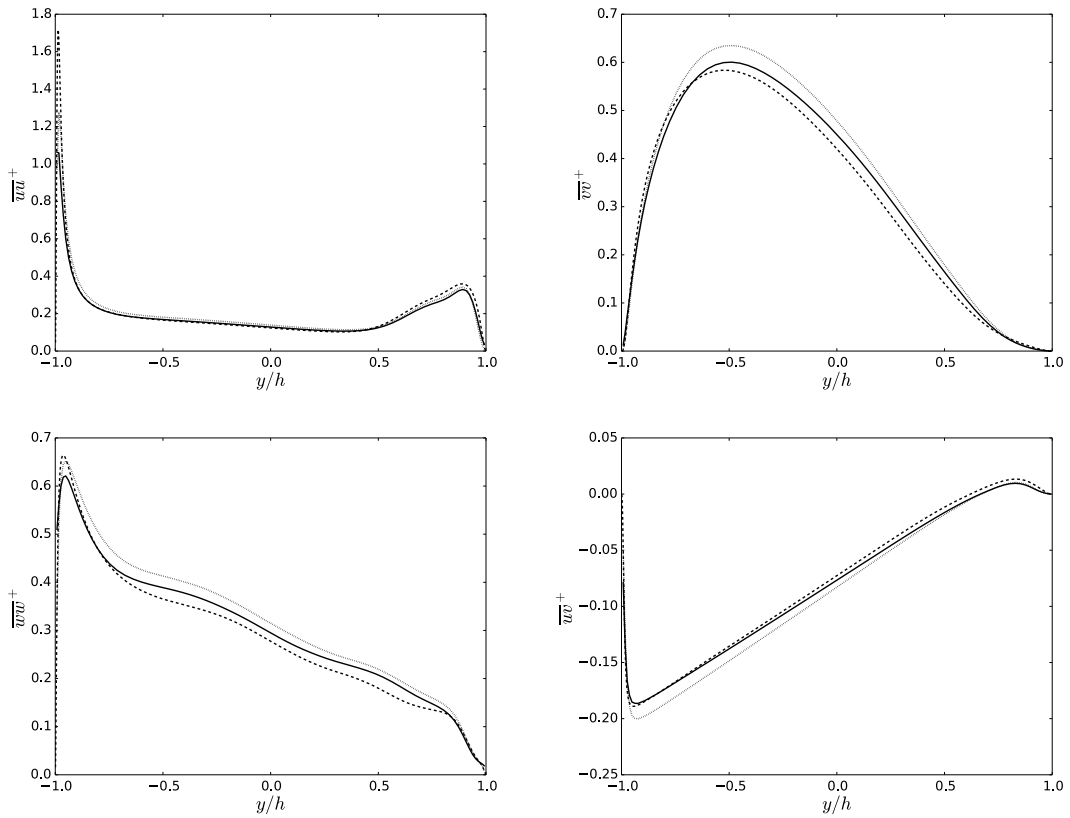


Figure 30: WMLES —, wall-resolved LES ---, under-resolved LES, ····. Reynolds stresses when  $Re \approx 20\,000$  and  $Ro = 0.45$ .

Figure 31 shows the instantaneous wall shear stress patterns for the WMLES case. These patterns behave as expected, as they are defined by the footprint of the instantaneous velocity field at the exchange location. From the figure it can be observed that the smaller structures are filtered on the pressure side, since the turbulence scales grow with increasing  $y$ . Similar trend can also be seen on the suction side, but also some smaller scale turbulence spots can be detected. However, these turbulent spots tend to follow the elongated ribbon shape structures, compared to more arbitrary shapes detected in the wall-resolved case. In addition, the wall-model is not able to maintain the periodic behavior of the shrinking and growing of these spots, and as a result the total shear stress deviations become random. The instantaneous wall shear stress patterns would naturally become even more filtered if the exchange location would be selected to be further away from wall.

Figure 32 shows the two-point correlations in the  $x$ - and  $z$ -directions close to the exchange location for the pressure and suction side, respectively. The wall-resolved correlations are visualized in the graphs for comparison. From these graphs, it can be observed that the wall-modeling does not essentially change structure of turbulence on the pressure side. The small deviations most likely result from the difference in the  $y$ -resolution. However, on the suction side the correlations clearly differ from the corresponding wall-resolved values, and support the fact that the periodic behavior of the intensive wall shear stress spots cannot be fully captured. Especially, the spanwise correlation for  $u'u'$  vanishes almost completely, which is associated with the transporting spanwise velocity fluctuations being filtered due to the wall-modeling. Despite the distortion of the turbulent structures at this complex semi-turbulent region, the correlations were found to be in good agreement further away from the wall when  $y_s^+ > 250$ .

The spectral density graphs of  $k_x E_{xx}$  were also studied to examine if the wall-model significantly changes the length scales of the most energetic turbulent structures, and these are presented in Figure 33. Overall the curves are in good agreement with the wall-resolved data and the primary observation is that the dynamically important scales in the outer layer are unaffected by the modeling. However, small differences can be noticed near the wall-model area on the pressure side, which is separately visualized in Figure 33b. The main observation is that the logarithmic slope is slightly more vague, as the trend of most energetic scales becoming larger seems to start slightly earlier. Nevertheless, there is no clear buffer layer where the most meaningful scales would be significantly distorted. Since the wall-model is not expected to capture real turbulence physics near the modeling region, the spectral results are in fact very promising and surprisingly good even in this region. The reason behind this beneficial behavior is most likely the weak coupling of the two zones.

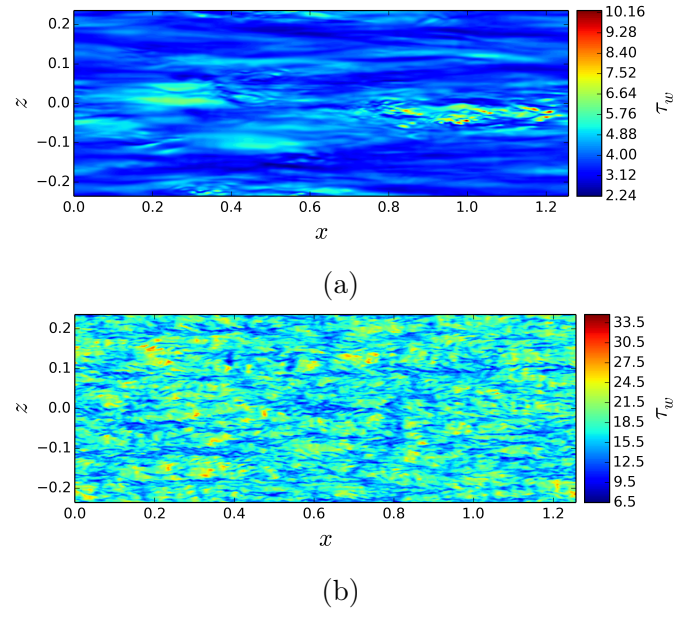


Figure 31: (a) Instantaneous wall shear stress field on the suction side when  $Re \approx 20000$  and  $Ro = 0.15$ , (b) Pressure side.

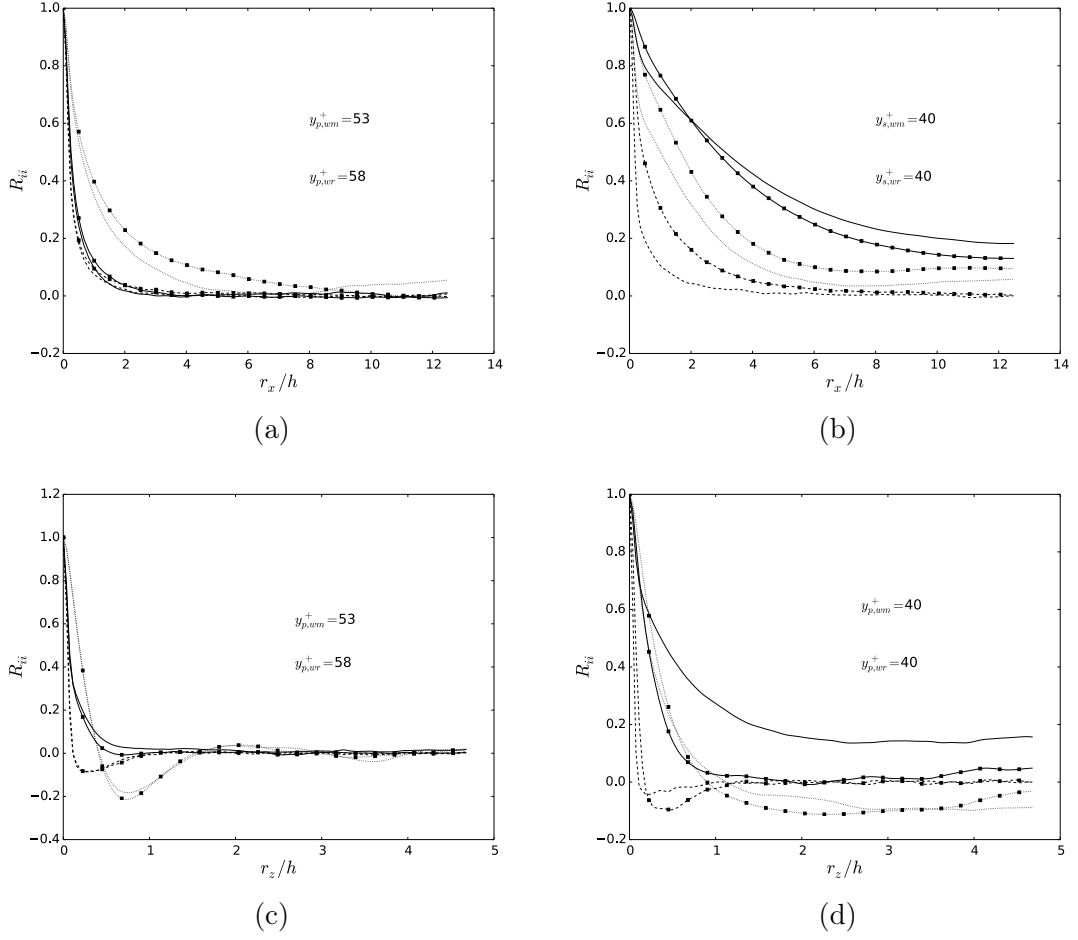


Figure 32:  $R_{uu}$  —,  $R_{vv}$  ---,  $R_{ww}$  ·····, Wall-modeled ■, Wall-resolved - no marker. Two-point correlations close to the wall-model interface.

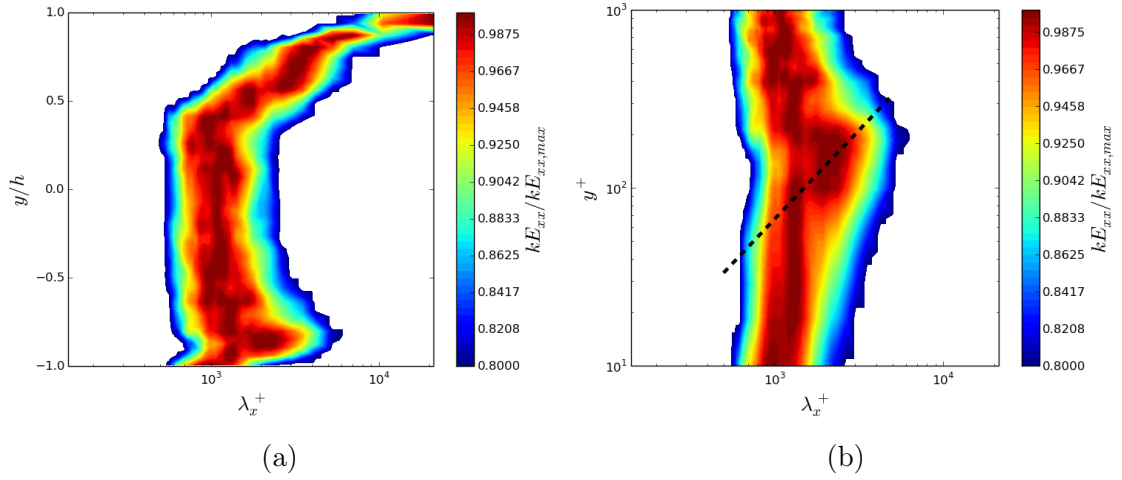


Figure 33: (a) Local spectral density of the turbulent kinetic energy  $k_x E_{xx}$  as a function of the length scale  $\lambda_x^+$  and the dimensionless  $y$ -coordinate for the WMLES  $Ro = 0.45$  case. Shaded isocontours represent the locally largest 20% red being the maximum. (b) Local spectral density of  $k_x E_{xx}$  as a function of local  $y^+$  for the pressure side.

## 9 Conclusions and Future Work

The results obtained in this study suggest that the Wall-Modeled Large Eddy Simulation is a viable approach for high Reynolds number rotating flows. However, since the traditional wall-models do not take the system rotation into account, they cannot be utilized without a modification. In general, the rotation modification can be done by adjusting the governing turbulence model within the wall-model layer to adapt to the local stability effects resulting from the Coriolis force.

In this study, we studied the auxiliary grid wall-modeling approach by Kawai and Larsson and modified the traditional mixing length turbulence model with a coefficient based on the local stability parameter, the gradient Richardson number. This modification was found to significantly enhance the results, the main improvement being the independence on the wall-model height. Another promising feature discovered in the project was that this kind of auxiliary grid approach does not change the turbulence physics in the outer layer probably due to the weak coupling of the two layers. This suggests that the approach might also be feasible for more complex geometries. However, instantaneous wall shear patterns cannot be considered as exact, since they are based on the velocity footprints at the exchange location and tend to become increasingly filtered with increasing wall-model height.

The main difficulty of this auxiliary grid method with the rotation corrected mixing length model is to find the correct van Driest damping constant  $A^+$  (dimensionless thickness of viscous sublayer), which is a function of Reynolds and rotation numbers. This feature is very difficult to avoid in any weakly coupled model, since most of the turbulence models reduce to the mixing length model near the wall, or require other user defined parameters. Therefore, replacing the mixing length model with another RANS type turbulence model does not seem promising. For now, a reasonable value for  $A^+$  could be found by performing a cheap preliminary simulation. In fact, the preliminary simulation generally is a good starting point, since it provides a guideline for the required mesh parameters as well.

A natural follow-up for this project would be to focus on studying the behavior of the dimensionless thickness of the viscous sublayer and thereby the optimal value of van Driest damping constant  $A^+$  as a function of Reynolds and rotation numbers. For this purpose it would be necessary to properly study the turbulence phenomena, which causes the decrease in the wall shear stress on the pressure side, although the turbulence is locally increased on the wall. The primary objective would be to find a property at the exchange location, which would dynamically adjust the value of  $A^+$ . Furthermore, strongly coupled RANS/LES hybrids would be an intriguing approach to examine, but they would also require a new type of trigger for the zone division. Another topic for the future work would be to extend the wall-model to include the effects of the wall (streamline) curvature in addition to the system rotation, which would be great improvement towards practical applications, such as turbomachinery. As there is a similar Richardson number based analogy for the curvature effects, the combined effect of rotation and curvature should be relatively straightforward to implement.

## References

- [1] Kristoffersen, R. & Andersson, H.I., “Direct simulations of low-Reynolds-number turbulent flow in a rotating channel,” *Journal of Fluid Mechanics*, vol. 256, pp. 163–197, 1993.
- [2] Kawai, S. & Larsson, J., “Wall-modeling in large eddy simulation: length scales, grid resolution and accuracy,” *Physics of Fluids*, vol. 24, 2012.
- [3] Smagorinsky, J., “General circulation experiments with the primitive equations,” *Monthly Weather Review*, vol. 91, pp. 99–164, 1963.
- [4] Childs, P.R.N, *Rotating Flow*. Elsevier, 2010. ISBN: 978-0-12-382098-3.
- [5] Hinze, J.O., *Turbulence: An Introduction to Its Mechanics and Theory*. McGraw-Hill, 1st ed., 1959. ISBN: 978-0070290389.
- [6] Chapman, D.R., “Computational aerodynamic development and outlook,” *AIAA*, vol. 17, no. 12, pp. 1293–1313, 1979.
- [7] S. Larsson, J. & Kawai, “Wall-modeling in large eddy simulation: length scales, grid resolution and accuracy,” *Center for Turbulence Research Annual Research Briefs, Stanford University*, 2010.
- [8] Hill, P.G. & Moon, I.M, “Effects of coriolis on the turbulent boundary layer in rotating fluid machines,” *MIT Gas Turbine Lab. Rep. 69*, 1962.
- [9] Moon, I.M, “Effects of coriolis on the turbulent boundary layer in rotating fluid machines,” *MIT Gas Turbine Lab. Rep. 74*, 1964.
- [10] Moore, J., “Effects of coriolis forces on turbulent flow in rotating channels,” *MIT Gas Turbine Lab. Rep. 69*, 1967.
- [11] Bradshaw, P., “The Analogy Between Streamline curvature and Buoyancy in Turbulent Shear Flow,” *Journal of Fluid Mechanics*, vol. 36, pp. 177–191, 1969.
- [12] Johnston, P.J. , Robert, M.H. & Lezius D.K., “Effects of spanwise rotation on the structure of two-dimensional fully developed turbulent channel flow,” *Journal of Fluid Mechanics*, vol. 56, pp. 533–557, 1972.
- [13] Kim, J., “The effect of rotation on turbulence structure,” *Proc 4th Sump on Turbulent Shear Flows, Karlsruhe*, 1983.
- [14] Miyake, Y. & Kajishima, T., “Numerical simulation of the effects of Coriolis force on the structure of turbulence,” *Bulletin of the Japan Society of Mechanical Engineering*, vol. 19, 1986.
- [15] Lamballais, E., Lesieur, M. & Métais, O., “Effects of spanwise rotation on the vorticity stretching in transitional and turbulent channel flow,” *International Journal of Heat and Fluid Flow*, vol. 17, pp. 324–332, 1996.

- [16] Alvelius, K., *Studies of turbulence and its modeling through large eddy- and direct numerical simulations*. PhD thesis, Royal Institute of Technology, Stockholm, 1999.
- [17] Wallin, S., Grundestam, O., Johansson, A.V., “Laminarization mechanisms and extreme-amplitude states in rapidly rotating plane channel flow,” *Journal of Fluid Mechanics*, vol. 730, pp. 193–219, 2013.
- [18] Deardorff, J.W., “A numerical study of three-dimensional turbulent channel flow at large Reynolds numbers,” *Journal of Fluid Mechanics*, vol. 41, pp. 453–480, 1970.
- [19] Schumann, U., “Subgrid scale model for finite difference simulations of turbulent flows in plane channels and annuli,” *Journal of Computational Physics*, vol. 18, pp. 376–404, 1975.
- [20] Grotzbach, G., “Direct numerical and large-eddy simulations of turbulent channel flows,” *Encyclopaedia of Fluid Mechanics*, ed. N.P. Cheremisinoff, vol. 6, pp. 1337–1391, 1987.
- [21] Balaras, E., Benocci, C. & Piomelli U., “Two-layer Approximate Boundary Conditions for Large-Eddy Simulations,” *AIAA Journal*, vol. 34, no. 6, pp. 1111–1119, 1996.
- [22] Wang, M. & Moin, P., “Dynamic wall modeling for large eddy simulation of complex turbulent flows,” *Physics of Fluids*, vol. 14, no. 7, 2002.
- [23] Spalart, P.R, Jou, W.H., Strelets, M., Allmaras, S.R., “Comments on the feasibility of LES for winds, and on a hybrid RANS/LES approach,” *Proceedings of the First AFOSR International Conference on DNS/LES*, 1997.
- [24] Strelets, M., “Detached Eddy Simulation of Massively Separated Flows,” *AIAA Meeting*, vol. 0879, 2001.
- [25] de Villiers, E., *The Potential of Large Eddy Simulation of the Modelling of Wall Bounded Flows*. PhD thesis, Imperial College of Science, Technology and Medicine - Department of Mechanical Engineering, July 2006.
- [26] Sagaut, P., *Large Eddy Simulation for Incompressible Flow*. Springer, 3rd ed., 2006. ISBN:13 978-3-540-26344-9.
- [27] Garnier, E., Adams, N. & Sagaut, P., *Large Eddy Simulation for Compressible Flows*. Springer, 2009.
- [28] Meng, N. & Pletcher, R.H., “Large Eddy Simulation of rotating channel flows with and without heat transfer,” *Proceedings of ASME, International Mechanical Engineering Congress & Exposition*, 2000.
- [29] Vreman, A.W., “An eddy-viscosity subgrid-scale model for turbulent shear flow: Algebraic theory and applications,” *Physics of Fluids*, vol. 16, no. 10, 2004.

- [30] Eidson, T.M., “Numerical simulation of the turbulent Rayleigh-Benard problem using subgrid modelling,” *Journal of Fluids Mechanics*, vol. 158, 1985.
- [31] Hadjadj, A., Ben-Nasr, O., Shadloo, M.S., Chaudhuri, A., “Effect of wall temperature in supersonic turbulent boundary layers: A numerical study,” *International Journal of Heat and Mass Transfer*, vol. 81, pp. 426–438, 2015.
- [32] Choi, H. & Moin, P., “Grid-point requirements for large eddy simulation: Chapman’s estimates revisited,” *Annual Research Briefs, Center for Turbulence Research*, 2011.
- [33] Jimenez, J., “Cascades in Wall-Bounded Turbulence,” *Annual Review of Fluid Mechanics*, vol. 44, pp. 27–45, 2012.
- [34] Piomelli U., Ferziger J.H, Moin P. and Kim, J., “New approximate boundary conditions for large eddy simulations of wall-bounded flows,” *Physics of Fluids A*, vol. 1, 1989.
- [35] Rajagopalan S. & Antonia, R.A., “Some properties of the large structure in a fully developed turbulent duct flow,” *Physics of Fluids*, 1979.
- [36] Balaras, E. & Benocci, C., “Subgrid-scale models in finite-difference simulations of complex wall bounded flows,” *AGARD CP*, vol. 551, 1994.
- [37] Pope, S.B., *Turbulent Flows*. Cambridge University Press, 2000.
- [38] Piomelli, U. & Balaras, E., “Wall-Layer models for Large-Eddy Simulations,” *Annual Review of Fluid Mechanics*, vol. 34, 2002.
- [39] Kawai, S. & Larsson, J., “Dynamic non-equilibrium wall-modeling for large eddy simulation at high Reynolds numbers,” *Physics of Fluids*, vol. 25, 2013.
- [40] Park, I.P. & Moin, P., “An improved dynamic non-equilibrium wall-model for Large Eddy Simulation,” *Physics of Fluids*, vol. 26, 2014.
- [41] Bodart, J. & Larsson, J., “Wall-modeled large eddy simulation in complex geometries with application to high-lift devices,” *Annual Research Briefs, Center for Turbulence Research, Stanford University*, 2011.
- [42] Piomelli, U., “Wall-layer models for large-eddy simulations,” *Progress in Aerospace Sciences*, vol. 44, 2008.
- [43] Spalart, P.R., Deck, S., Shur M.L., Squires, K.D., Strelets, M.K., Travin, A., “A new version of detached-eddy simulation, resistant to ambiguous grid densities,” *Theoretical and Computational Fluid Dynamics*, vol. 20, pp. 181–195, 2006.
- [44] Shur, M.L, Spalart, P.R., Strelets, M.K, Travin, A.K., “A Hybrid RANS-LES Approach With Delayed-DES and Wall-Modelled LES Capabilities,” *International Journal of Heat and Fluid Flow*, vol. 29, p. 1638–1649, 2008.

- [45] Larsson J., Lien F.S., Yee E., “The artificial buffer layer and the effects of forcing in hybrid LES/RANS,” *International Journal of Heat and Fluid Flow*, vol. 28, pp. 1443–1459, 2007.
- [46] Adams, R.A. & Essex, C., *Calculus: A Complete Course*. Pearson, 7th ed., 2010. ISBN: 978-0-321-54928-0.
- [47] Brethower, G., Schlatter, P. and Johansson, A.V., “Turbulence, instabilities and passive scalars in rotating channel flow,” *Journal of Physics: Conference Series*, vol. 318, 2011.
- [48] Bermejo-Moreno, I., Campo, L., Larsson, J., Bodart, J., Helmer, D. and Eaton, J.K., “Confinement effects in shock wave/turbulent boundary layer interactions through wall-modeled large-eddy simulations,” *Journal of Fluid Mechanics*, vol. 758, pp. 5–62, 2014.
- [49] Watmuff, J.H., Witt, H.T. and Joubert, P.N., “Developing turbulent boundary layer with system rotation,” *Journal of Fluid Mechanics*, vol. 157, 1985.
- [50] Jimenez, J., Wray, A.A., Saffman, P.G. and Rogallo, S.R., “The structure of intense vorticity in isotropic turbulence,” *Journal of Fluid Mechanics*, vol. 255, pp. 65–90, 1993.
- [51] Howard, J.H.G., Patankar, S.V. and Bordyniuk, R.M., “Flow Prediction in Rotating Ducts Using Coriolis-Modified Turbulence Models,” *Journal of Fluids Engineering*, vol. 102, 1980.